UNIVERSITY OF TRENTO

Doctoral School in Civil, Environmental and Mechanical Engineering

Curriculum 3. Modelling and Simulation

Daniel Kempen

Thermomechanical modelling of powder compaction and sintering

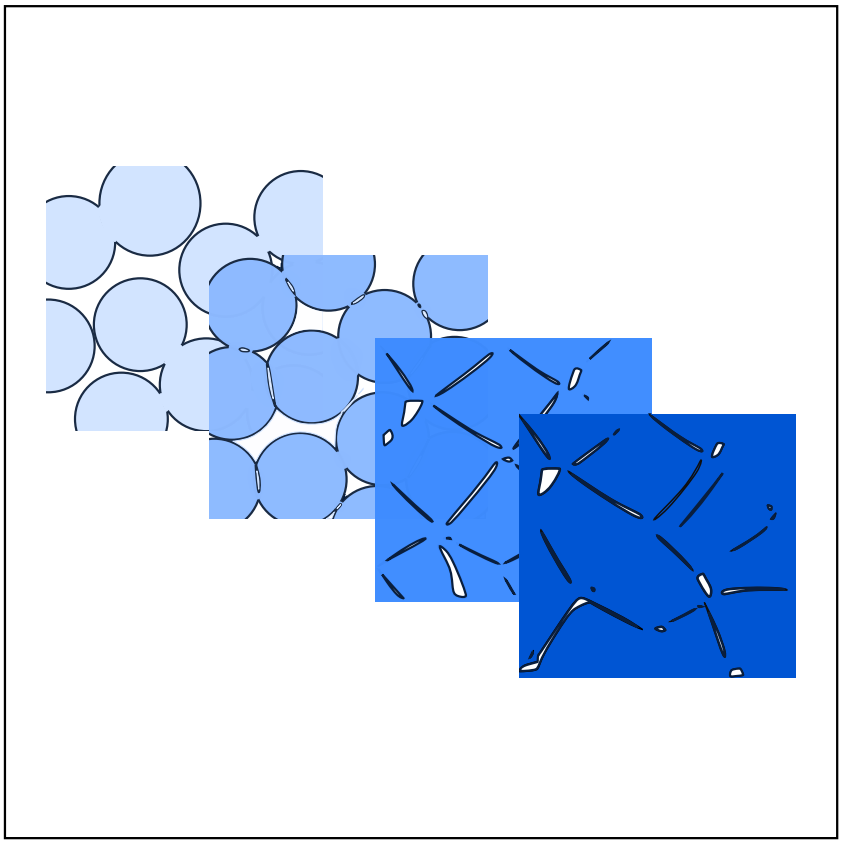

2019 - Doctoral thesis

University of Trento

Thermomechanical modelling of powder compaction and sintering

Author:
Daniel Kempen

Supervisors:
prof. Andrea Piccolroaz
prof. Davide Bigoni

UNIVERSITY OF TRENTO

University of Trento
Doctoral School in Civil, Environmental and Mechanical Engineering
http://web.unitn.it/en/dicam
Via Mesiano 77, I-38123 Trento
Tel. +39 0461 282670 / 2611 - *dicamphd@unitn.it*

Acknowledgements

I would like to express my gratitude to prof. Andrea Piccolroaz for giving me the chance to participate in this research project. I would like to thank him for his support and help while simultaneously leaving me the freedom to pursue my research.
I would like to thank prof. Davide Bigoni for his help, for encouraging me and for the many suggestions that added substantial value to my research. I am very grateful that they gave me the opportunity to pursue a PhD in Italy at the University of Trento.

I am also indebted to Claudio Ricci from Sacmi (Imola) for his great help with the experiments that we performed in the R&D laboratories of Sacmi. I would also like to thank Dr. Simone Sprio, from CNR-Istec (Faenza), who was so kind to help me with the specimen preparation for the experiments with ceramic cylinders. Many thanks to Dr. Séverine Romero Baivier from Vesuvius, who hosted me for my secondment in Belgium and gave me the possibility to perform the triaxial tests at the laboratory of Vesuvius.
I want to thank prof. Rebecca Brannon from the University of Utah, who helped me discussing some of the numerical problems of this work.

I want to also thank my fellow doctoral students from the Marie Curie "Cermat2" for the good times we had during the meetups and conferences that we attended together: Gennaro Vitucci, Domenico Tallarico , Nikolai Gorbushin, Shwetank Pandey, Mojtaba Biglar. And of course a special thanks goes to my collegue in Trento Scot Swan (also from Cermat2) with whom I had many useful discussions around programming and material modeling.

The project was financed by the FP7-PEOPLE-2013-ITN Marie

Curie ITN transfer of knowledge program (PITN-GA-2013-606878-CERMAT2). I am very grateful for this financial support as without it, I would not have had the great opportunity to pursue my PhD in Italy, visit conferences or Summer/Winter schools.

Published Material

The content of this thesis is, in parts, published in:

D. Kempen, A. Piccolroaz, D. Bigoni. "Thermomechanical modelling of ceramic pressing and subsequent sintering" In: *Journal of Mechanical Sciences* (*submitted*)

D. Kempen, A. Piccolroaz, D. Bigoni. "Thermomechanical modelling of powder compaction and ceramic sintering" *Proceedings of the workshop for young ceramists*, 2018, ISBN: 978-88-7586-599-3

Contents

List of Tables

List of Figures

Abstract

An elastic-visco-plastic thermomechanical model for cold forming of ceramic powders and subsequent sintering is introduced and based on micromechanical modelling of the compaction process of granulates. Micromechanics is shown to yield an upper-bound estimate to the compaction curve of a granular material, which compares well with other models and finite element simulations. The parameters of the thermomechanical model are determined on the basis of available data and dilatometer experiments. Finally, after computer implementation, validation of the model is performed with a specially designed ceramic piece showing zones of different density. The mechanical model is found to accurately describe forming and sintering of stoneware ceramics and can therefore be used to analyze and optimize industrial processes involving compaction of powders and subsequent firing of the greens.

1 Introduction

1.1 Sintering

Sintering is a thermal process that is used to bond particles together, so that they form a solid. This technique is used since at least 8000 years [35] to form bodies from clay and has undergone enormous development since then [24]. One of the main advantages of sintering is that the powder can be easily put into shape, and then through firing the strength of the body increases dramatically. Thus, it is possible to create a body from a high strength material with rather complex geometries. If one had to cut, lathe, mill or drill the shape out of solid cube of this material, much more effort would be required. A main disadvantage of sintering has to do with the very same effect. The body is initially a powder compact, with lots of void space between the particles. During the sintering the particles grow together to form a compact of a higher density, but this means also, that the body shrinks in dimension. Due to the shrink the final geometry is not the same as the initial geometry of the powder compact. It is not easy to predict the shrink beforehand. If the resultant body is supposed to have certain dimensions, it is not straightforward to tell the dimensions of the powder compact. There are certain strategies to obtain a sintered part in the desired dimension. One possibility is to machine the part after sintering. This is the most commonly used method for precision parts as of now. But a substantial amount of work is required. Also this process goes hand-in-hand with wear of tooling etc., as sintered bodies are often made from very hard materials. It would be thus very desirable to be able to predict the final shape already in advance. This is called net-shape manufacturing. However, as true net-shape production is not yet possible one speaks most of the time of near-net-shape manufacturing.

1.2 Modelling of ceramic production processes

The production of ceramic pieces is based on technologies involving a massive waste of energy and materials*, so that environmental preservation imposes a rationalization of industrial processes to reduce pollution. The optimization of the production process is directly linked to the modelling of the mechanical behavior of powders and binders used during compaction, in the simulation of cold compaction and subsequent sintering, and in the design of mechanical characteristics of the final pieces.

Sintering is the common method for completing the process of ceramic production and involves heating of the green bodies, obtained in the preceding compaction stage, to obtain the required density and strength of the final products. Understanding and modelling the mechanisms involved in the sintering process is therefore crucial to ensure high quality and reproducibility of ceramic materials.

In the last 50 years, there have been significant developments in the theory of sintering but only in the 1980s the use of continuum mechanics was introduced, to predict the stresses and strain that can develop during the process. A comprehensive review of the models for sintering proposed in the last 25 years can be found in [25]. In recent years, meso-scale models have been developed using multi particle Finite Element (MPFEM) approaches [49] or discrete element approaches [59]. These models are useful in the understanding of micro or mesomechanical effects, but due to the limited particle number it is difficult to model whole complex

* Grinding of the raw material requires mills with a power up to 1 MW, drying and increasing of the temperature of the slip involves up to 500 KW of electrical power and 15 Gcal/h of thermal power. The 80% of the thermal capacity is lost at the chimney and powder is spread in the environment. The forming of the ceramic powders is a huge waste of energy, since only the 5% of the energy is transmitted to the final piece from the presses (up to 250 KW of installed power). Finally, drying and sintering requires large burners consuming up to 10 Gcal/h.

shaped parts, so that continuum models, such as those developed in [1, 16, 46], play a central role.

Often sintering was studied with reference to isothermal conditions [38, 46], but during the firing the body is subject to non-isothermal loadings, especially for high heating rates and larger parts, so that the modelling of this situation is an objective of the present thesis.

Before sintering, a green body is obtained through powder compaction and, depending on the geometry and the compaction method, the pressed green body shows usually significant differences of local density throughout the part [56]. Therefore, powder pressing has a strong influence on sintering, which depends on the (relative) density of the green.

Therefore a continuum model that can predict the density distribution after the pressing step and the subsequent sintering would be important for industrial applications. In this research direction, while cold compaction has been often addressed [13, 17, 18, 39, 48, 52], the combination of pressing and sintering has been scarcely investigated. In particular, two different models, one for powder pressing and another for sintering have been proposed [38], while thermomechanical models for hot-isostatic pressing of metal powders were developed using a pressure-sensitive and temperature dependent yield function [20, 41].

The objective of the present thesis is to propose a thermomechanical, elastic-visco-plastic model to simulate cold powder compaction and subsequent non-isothermal solid state sintering. The model is grounded on the thermomechanical framework developed by Simo and Miehe [43, 55] and on the additive decomposition of elastic and plastic logarithmic strains [43, 53]. Moreover, the BP yield function [7] is used to simulate both compaction and firing, so that these two process steps become more closely integrated. With reference to an aluminum silicate spray dried powder (used for the industrial production of ceramic tiles), the model is calibrated against *ad-hoc* performed experiments and

implemented (through an UMAT routine) in a finite element code (Abaqus). Finally, validation against an experiment performed on a large ceramic piece (in which density variations were intentionally introduced) shows that the model provides an accurate prediction of the entire process of forming and sintering. The model remains therefore available for the design and optimization of ceramic pieces.

2 Continuum Mechanics

2.1 Kinematics

For the study of kinematics, we consider a body that has a reference configuration $\mathcal{B}_0$ and a deformed (or current) configuration $\mathcal{B}$. A single material point within the body in the reference configuration is denoted by $\boldsymbol{x}$, whereas a material point in the current configuration is denoted by $\boldsymbol{y}$. For simplicity we always assume a cartesian coordinate system. Treatments of the topic of curvilinear cartesian systems can be found e.g in [33]. The motion of the body can be described by a transformation φ.

$$\boldsymbol{y} = \varphi(\boldsymbol{x}) \tag{1}$$

2.1.1 Deformation Gradient

The deformation gradient $\boldsymbol{F}$ is defined as the gradient of the transformation φ (see [6, 14, 15]) :

$$\boldsymbol{F} = \nabla\varphi(\boldsymbol{x}) = \nabla\left(\boldsymbol{x} + \boldsymbol{u}(\boldsymbol{x})\right) = \boldsymbol{I} + \nabla\boldsymbol{u}(\boldsymbol{x}). \tag{2}$$

It gives a relationship between a material fiber in the current configuration and in the deformed configuration

$$d\boldsymbol{y} = \boldsymbol{F}\, d\boldsymbol{x}. \tag{3}$$

Relationship 3 can be derived (following [10]) by considering the line element $d\boldsymbol{x}$ in the deforming solid as pictured in Figure 1. The undeformed configuration $\mathcal{B}_0$ is shown on the left and the deformed configuration $\mathcal{B}$ on the right. The infinitesimally small line element $d\boldsymbol{y}$ can be expressed as:

$$d\boldsymbol{y} = \boldsymbol{x} + d\boldsymbol{x} + \boldsymbol{u}(\boldsymbol{x} + d\boldsymbol{x}) - (\boldsymbol{x} + \boldsymbol{u}(\boldsymbol{x})) \tag{4}$$

We can expand $\boldsymbol{u}(\boldsymbol{x} + d\boldsymbol{x})$ as a Taylor series:

$$\boldsymbol{u}(\boldsymbol{x} + d\boldsymbol{x}) = \boldsymbol{u}(\boldsymbol{x}) + \frac{\partial \boldsymbol{u}}{\partial \boldsymbol{x}} d\boldsymbol{x} + \mathcal{O}(\boldsymbol{x}^2), \tag{5}$$

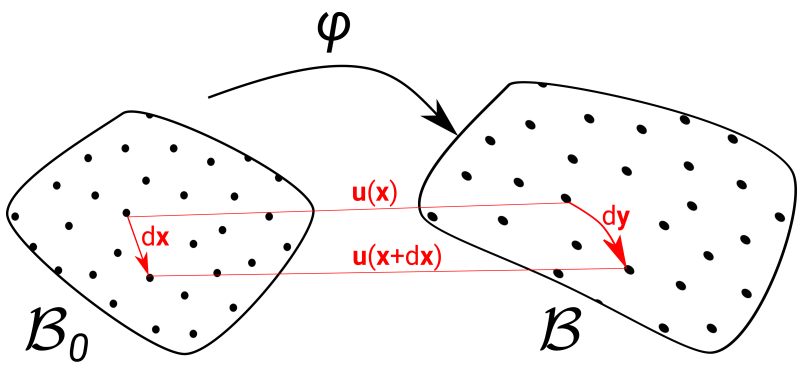

Figure 1: Transformation of an infinitesimal line element $d\boldsymbol{x}$ from the reference configuration (left) into the current configuration (right).

and upon insertion of eq.(5) into eq.(4) we gain:

$$\begin{aligned} d\boldsymbol{y} &= \boldsymbol{x} + d\boldsymbol{x} + \boldsymbol{u}(\boldsymbol{x}) + \frac{\partial \boldsymbol{u}}{\partial \boldsymbol{x}} d\boldsymbol{x} + \mathcal{O}(\boldsymbol{x}^2) - (\boldsymbol{x} + \boldsymbol{u}(\boldsymbol{x})) \\ &= d\boldsymbol{x} + \frac{\partial \boldsymbol{u}}{\partial \boldsymbol{x}} d\boldsymbol{x} + \mathcal{O}(\boldsymbol{x}^2) = (\boldsymbol{I} + \frac{\partial \boldsymbol{u}}{\partial \boldsymbol{x}}) d\boldsymbol{x} + \mathcal{O}(\boldsymbol{x}^2). \end{aligned} \tag{6}$$

After insertion of eq.(2) into eq.(6) it yields:

$$d\boldsymbol{y} = \boldsymbol{F} d\boldsymbol{x} + \mathcal{O}(\boldsymbol{x}^2). \tag{7}$$

Finally, for infinitesimally small pieces, we can neglect higher order terms and as a result we gain eq.(3).

2.1.2 Differential Volume Element

If we imagine a parallelepiped volume element in the reference configuration at point $\boldsymbol{x}$ that has three base vector $d\boldsymbol{a}$, $d\boldsymbol{b}$ and $d\boldsymbol{c}$, then we can express its volume as:

$$dV_0 = (d\boldsymbol{a} \times d\boldsymbol{b}) \cdot d\boldsymbol{c}. \tag{8}$$

In the current configuration each of the base vectors is mapped according to eq. (3). It follows that the volume of the mapped volume element can be expressed by:

$$dV = (\boldsymbol{F}d\boldsymbol{a} \times \boldsymbol{F}d\boldsymbol{b}) \cdot \boldsymbol{F}d\boldsymbol{c}. \tag{9}$$

The ratio of the two volumes in current and reference configuration is equal to the determinant of the deformation gradient (see [14, 33]):

$$\frac{dV}{dV_0} = \frac{(\boldsymbol{F}d\boldsymbol{a} \times \boldsymbol{F}d\boldsymbol{b}) \cdot \boldsymbol{F}d\boldsymbol{c}}{(d\boldsymbol{a} \times d\boldsymbol{b}) \cdot d\boldsymbol{c}} = \det \boldsymbol{F} \tag{10}$$

The determinant of the deformation gradient is therefore a measure for volume change of the body and as such an important quantity for many constitutive models. It is usually denoted by:

$$J = \det \boldsymbol{F}. \tag{11}$$

2.1.3 Differential surface element

We imagine a differential surface element, that is defined by two vectors $\boldsymbol{v}_0$ and $\boldsymbol{w}_0$, and by the unit normal vector $\boldsymbol{n}_0$ that is orthogonal to $\boldsymbol{v}_0$ and $\boldsymbol{w}_0$. Then for the area A_0 we can state

$$dA_0\boldsymbol{n}_0 = \boldsymbol{v}_0 \times \boldsymbol{w}_0. \tag{12}$$

For the area of the transformed surface element in the current configuration $\boldsymbol{B}$ and taking into account eq. (3) we can state:

$$dA\boldsymbol{n} = \boldsymbol{F}\boldsymbol{v}_0 \times \boldsymbol{F}\boldsymbol{w}_0, \tag{13}$$

where $\boldsymbol{n}$ is the unit normal vector of the current configuration. It is possible to factor out $\boldsymbol{F}$ using some algebra (see [6]), to obtain:

$$\boldsymbol{F}\boldsymbol{v}_0 \times \boldsymbol{F}\boldsymbol{w}_0 = (\det \boldsymbol{F})\boldsymbol{F}^{-T}(\boldsymbol{v}_0 \times \boldsymbol{w}_0). \tag{14}$$

Finally by taking into consideration eq.(11) and inserting eq.(12) and eq.(13) into eq.(14), we obtain Nanson's rule of area transformation (for more on this see e.g. [6, 14, 45])

$$dA\boldsymbol{n} = J\boldsymbol{F}^{-T}\boldsymbol{n}_0 dA_0. \tag{15}$$

2.2 Strain Measures

2.2.1 Polar decomposition and stretches

According to the spectral decomposition theorem [33] it is possible to decompose a tensor (with positive determinant), e.g. the deformation gradient, into an orthogonal tensor $\boldsymbol{R}$ and a symmetric, positive definite tensor:

$$\boldsymbol{F} = \boldsymbol{R}\boldsymbol{U} = \boldsymbol{V}\boldsymbol{R}. \tag{16}$$

The orthogonal tensor $\boldsymbol{R}$ is called rotation tensor whereas $\boldsymbol{U}$ and $\boldsymbol{V}$ are called right and left stretch tensors.

2.2.2 Eigenvalue Problem

The eigenvalues λ of a tensor $\boldsymbol{A}$ are defined as the solutions of:

$$\boldsymbol{A}\boldsymbol{a} = \lambda\boldsymbol{a}, \quad \forall \boldsymbol{a} \neq \boldsymbol{0}. \tag{17}$$

By mapping the eigenvalue problem of eq. (17) several times by $\boldsymbol{A}$, we obtain:

$$\boldsymbol{A}^k\boldsymbol{a} = \lambda^k\boldsymbol{a}, \quad k = 1, 2, ... \tag{18}$$

This leads to the spectral mapping theorem (more on this can be found in [33]), that allows us to define for the polynomial function $g(\boldsymbol{A}) = \sum_{k=0}^{m} a_k \boldsymbol{A}^k$ (using 18):

$$g(\boldsymbol{A})\boldsymbol{a} = \sum_{k=0}^{m} a_k \boldsymbol{A}^k \boldsymbol{a} = \sum_{k=0}^{m} a_k \lambda^k \boldsymbol{a} = g(\lambda)\boldsymbol{a}, \tag{19}$$

so that $g(\lambda) = \sum_{k=0}^{m} a_k \lambda^k$ is the eigenvalue of $g(\boldsymbol{A})$.

2.2.3 Spectral Decomposition

The spectral decomposition of a second order tensor $\boldsymbol{A}$ is given by (see [33]):

$$\boldsymbol{A} = \sum_{i=1}^{s} \lambda_i \sum_{k=1}^{r_i} \boldsymbol{a}_i^{(k)} \otimes \boldsymbol{b}_i^{(k)} = \sum_{i=1}^{s} \lambda_i \boldsymbol{P}_i, \tag{20}$$

where $\boldsymbol{P}_i$ is called eigenprojection tensor, and is generally complex. The vectors $\boldsymbol{a}$ and $\boldsymbol{b}$ are eigenvectors.The spectral representation (the right hand side of eq. 20) is often used to calculate tensor powers:

$$\exp(\boldsymbol{A}) = \sum_{i=1}^{s} \exp(\lambda_i) \boldsymbol{P}_i, \tag{21}$$

which is well-suited for finite-strain plasticity algorithms [5, 14]. The sum of the eigenprojection tensors over all three dimensions gives unity (see [33]):

$$\sum_{i=1}^{3} \boldsymbol{P}_i = \boldsymbol{I} \tag{22}$$

2.2.4 One-dimensional strain measures

The length variation in the reference configuration dL can be given by [4]:

$$dL = \sqrt{d\boldsymbol{x} \cdot d\boldsymbol{x}} \tag{23}$$

and the length variation dl in the current configuration can be given by:

$$dl = \sqrt{d\boldsymbol{y} \cdot d\boldsymbol{y}}. \tag{24}$$

The length ratio or also called stretch for a one-dimensional problem can be given by:

$$\lambda = \frac{dl}{dL} = \frac{\sqrt{d\boldsymbol{y} \cdot d\boldsymbol{y}}}{\sqrt{d\boldsymbol{x} \cdot d\boldsymbol{x}}}. \tag{25}$$

The strain measure for the small-strain theory is given by:

$$\frac{dl - dL}{dL} = \lambda - 1, \tag{26}$$

where the case of no deformation corresponds to a strain measure of zero. It is possible to think of other types of strain measures. However, it is desirable that the strain measure remains zero at zero deformation and is compatible with the small-strain theory. We imagine a strain measure ϵ as a function of the stretch λ:

$$\epsilon = f(\lambda). \tag{27}$$

A Taylor expansion of eq.(27) around $\lambda = 1$ gives:

$$f(\lambda) = f(1) + \frac{df}{d\lambda}(1)(\lambda - 1) + \frac{1}{2}\frac{d^2 f}{d\lambda^2}(1)(\lambda - 1)^2 + \mathcal{O}((\lambda - 1)^3) \tag{28}$$

If we think of a small-strain case, the terms of higher order would vanish, so we want our strain measure to be equal to the first-order term $(\lambda - 1)$, for small-strains. Also, it should rise monotonically, with increasing strain and be zero for unstrained $(\lambda = 1)$ states, so it should respect the following conditions:

$$f(1) = 0; \quad \frac{df}{d\lambda}(1) = 1; \quad \frac{df}{d\lambda} > 0 \quad \forall \lambda > 0. \tag{29}$$

There are unlimited solutions to the problem and many different types of strain measures are used in continuum mechanics. Some of the more popular ones are:

$$\begin{aligned} \text{Nominal Strain:} \quad & f(\lambda) = \lambda - 1 \\ \text{Green's strain:} \quad & f(\lambda) = \frac{1}{2}(\lambda^2 - 1) \\ \text{Logarithmic Strain:} \quad & f(\lambda) = \ln(\lambda), \end{aligned} \tag{30}$$

which are plotted in Figure 2, for comparison. The logarithmic strain is popular for computational plasticty and many commercial FEM solvers, e.g. Abaqus use it for large-strain plasticity.

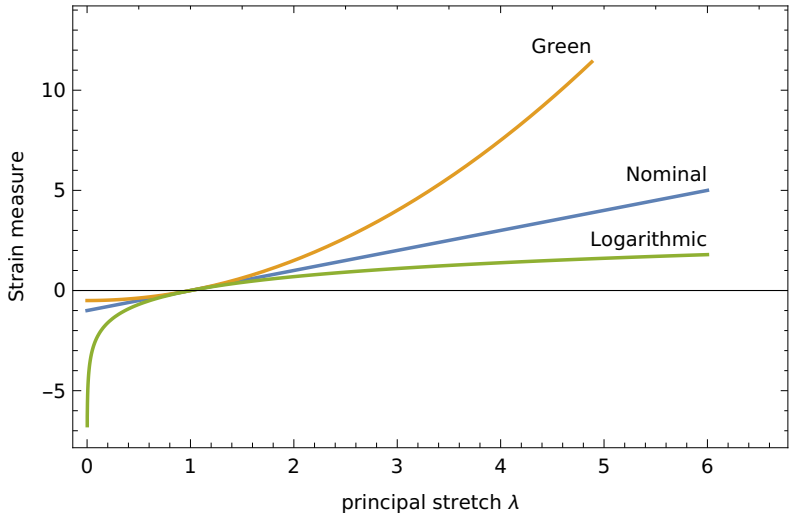

Figure 2: Various strain measures plotted against principal stretch.

2.2.5 Three-dimensional strains

For the three dimensional case, the solutions of chapter 2.2.4 can be generalized using the concept of the spectral decomposition from chapter 2.2.3. As a tensor can be expressed as the product of its eigenvalues times the projection tensors it is possible to write a strain measure $\boldsymbol{\epsilon}$ as:

$$\boldsymbol{\epsilon} = \sum_{i=1}^{3} \lambda_i \boldsymbol{P}_i = \sum_{i=1}^{3} \lambda_i \boldsymbol{a}_i \otimes \boldsymbol{b}_i, \tag{31}$$

If we restrict ourselfs to orthonormal bases (which is the case for carthesian coordinate systems), the eigenvectors become the principal direction of the coordinate system. For a system in the current configuration we denote the eigenvectors by $\boldsymbol{N}_i$ and for the reference configuration by $\boldsymbol{n}_i$. For the same choice of $f(\lambda)$ we can now define a famly of strains in the current configuration

(denoted by $\boldsymbol{E}$)

$$\begin{aligned}
\boldsymbol{E}^{(0)} &= \sum_{i=1}^{3} \ln(\lambda_i) \boldsymbol{N}_i \otimes \boldsymbol{N}_i. \quad \text{Logarithmic/Hencky strain} \\
\boldsymbol{E}^{(1)} &= \sum_{i=1}^{3} (\lambda_i - 1) \boldsymbol{N}_i \otimes \boldsymbol{N}_i. \quad \text{Biot/Nominal strain} \\
\boldsymbol{E}^{(2)} &= \sum_{i=1}^{3} \frac{1}{2} (\lambda_i^2 - 1) \boldsymbol{N}_i \otimes \boldsymbol{N}_i \quad \text{Green-Lagrange strain,}
\end{aligned} \tag{32}$$

where the upper index in parenthesis is just and index and not an exponent. It is not always convenient to calculate the strains with the above formulas, as the calculation of the eigenvalues is required. Instead, the strains are often times calculated by using the deformation gradient, or the stretch tensors (see eq. (16)). Using the definition of the right stretch tensor ([45]):

$$\boldsymbol{U} = \sum_{i=1}^{3} \lambda_i \boldsymbol{N}_i \otimes \boldsymbol{N}_i \tag{33}$$

and eq.(22) one can express the strain measure from eq. (32) as:

$$\begin{aligned}
\boldsymbol{E}^{(0)} &= \ln(\boldsymbol{U}) \quad \text{Logarithmic/Hencky strain} \\
\boldsymbol{E}^{(1)} &= \boldsymbol{U} - \boldsymbol{I} \quad \text{Biot/Nominal strain} \\
\boldsymbol{E}^{(2)} &= \frac{1}{2} (\boldsymbol{U}^2 - \boldsymbol{I}) \quad \text{Green-Lagrange strain,}
\end{aligned} \tag{34}$$

2.3 Stress measures

For nonlinear problems, such as finite-strain plasticity, various stress measures can be defined. In the following the most important ones for problems in plasticity are considered.

2.3.1 Cauchy stress tensor

If a surface load with resultant force ΔF acts on a limited surface ΔS of a body, with unit outward normal $\boldsymbol{n}$, the so-called traction vector $\boldsymbol{t}$ is defined as the limit of force over area [34]:

$$\boldsymbol{t_n} = \lim_{\Delta S \to 0} \frac{\Delta F}{\Delta S}. \tag{35}$$

The so-called Cauchy stress tensor (denoted by $\boldsymbol{\sigma}_c$) is defined as a second-order tensor that maps the stress components linearly onto the Cauchy stress vector:

$$\boldsymbol{t_n} = \boldsymbol{\sigma}_c \cdot \boldsymbol{n}. \tag{36}$$

the Cauchy stress tensor is often called true stress and is a measure for stress in the current configuration.

2.3.2 Nominal stress

If a uniaxial force F is applied to a body, with a constant cross section A_0 (e.g. a cylinder), the nominal stress is given by:

$$P = \frac{F}{A_0}, \tag{37}$$

which is the stress with respect to the reference configuration. The stress in the current configuration, called Cauchy stress is given by:

$$\sigma_c = \frac{F}{A}. \tag{38}$$

To generalize the concept of the nominal stress to three-dimensional stress states we can use Nanson's formula (eq. (15)) multiply both sides with the Cauchy stress vector $\boldsymbol{\sigma}_c^T \cdot \boldsymbol{n}$ and obtain:

$$\boldsymbol{t} dA = \boldsymbol{\sigma}_c^T \cdot \boldsymbol{n} dA = \boldsymbol{\sigma}_c^T J \boldsymbol{F}^{-T} \boldsymbol{n}_0 dA_0. \tag{39}$$

By comparing the equation one realizes that the factor $\boldsymbol{\sigma}_c^T J \boldsymbol{F}^{-T}$ on the right maps the Cauchy stress in the current configuration

to the reference configuration. This factor is called first Piola-Kirchhoff stress and denoted by $\boldsymbol{P}$:

$$\boldsymbol{P} = J\boldsymbol{\sigma}_c^T \boldsymbol{F}^{-T}, \tag{40}$$

whereas its transpose $\boldsymbol{P}^T$ is the nominal stress for three-dimensional problems:

$$\boldsymbol{P}^T = J\boldsymbol{F}^{-1} \cdot \boldsymbol{\sigma}_c. \tag{41}$$

2.3.3 Kirchhoff stress

The Kirchhoff stress $\boldsymbol{K}$ is defined by:

$$\boldsymbol{K} = J\boldsymbol{\sigma}_c. \tag{42}$$

The Kirchhoff stress is very similar to the Cauchy stress, the difference being that it is scaled by the determinant of the Jacobian J. This is why it is also called the weighted Cauchy stress.

2.4 Work-conjugate pairs

For the solution of problems of continuum mechanics over complex domains, the finite element method is a popular tool. The finite element method is used to solve the weak integral form. The theorem of virtual power is the weak form of the cauchy equation of motion and is the central equation for the solution of continuum mechanics problems. The equation includes an integral of the "stress-power" over the domain. The stress power or also called internal energy rate is the amount of energy that is transmitted to a unit volume element in terms of strain and stress [5]. It is possible to select different measure of stress and strains, but one needs to consider that the weak form of the integral is only valid, if the product of stress and strain gives indeed the stress-power. Pairs of strain and stresses that yield the stress-power for all possible paths of infinitesimal (virtual-) work are called work conjugate (the concept was introduced for

continuum mechanics by R. Hill [29]). The stress power, over an infinitesimal volume element dv in current configuration and dV in reference configuration is given by:

$$\int_{P_t} \boldsymbol{\sigma}_c : \boldsymbol{D}(\boldsymbol{v})\, dv = \int_{P_0} (J\boldsymbol{\sigma}_c) : \boldsymbol{D}(\boldsymbol{v})\, dV, \tag{43}$$

where $\boldsymbol{D}$ is the Eulerian strain rate, P_0 being a generic part of the body in the reference configuration and P_t the corresponding part in the current configuration. So the definition of work-conjugate stress and strain pairs is, that their scalar product is equal to $\boldsymbol{\sigma}_c : \boldsymbol{D}(\boldsymbol{v})$. Work-conjugate are the strains and stresses of the Seth-Hill family (more information on this can be found in [45]).

For the development of numerical plasticty models, which is the underlying aim of this thesis' research topic, usually the logarithmic strain measure is preferred. The work-conjugate to the logarithmic strain is the Kirchhoff stress, but only if the material is isotropic [29]. It is of importance as most simulation software (e.g. Abaqus) uses this measure for its internal calculations.

3 Thermoinelastic model for the sintering of ceramics

With the purpose of introducing a model for sintering of green ceramics, the large deformation of a thermo-elastic-visco-plastic solid is considered, described by the deformation gradient $\boldsymbol{F}$, the right and left Cauchy-Green tensors

$$\boldsymbol{C} = \boldsymbol{F}^T\boldsymbol{F}, \qquad \boldsymbol{B} = \boldsymbol{F}\boldsymbol{F}^T, \tag{44}$$

(where the superscript T denotes the transpose) and the corresponding Lagrangian and Eulerian logarithmic strains

$$\boldsymbol{\epsilon} = \frac{1}{2}\log \boldsymbol{C}, \qquad \boldsymbol{G}^{(0)} = \frac{1}{2}\log \boldsymbol{B}. \tag{45}$$

A key assumption is the additive decomposition of logarithmic strain into an elastic (subscript 'e') and a visco-plastic (subscript 'p') component proposed by Miehe et al. [43] and Sansour and Wagner [53] as

$$\boldsymbol{\epsilon} = \boldsymbol{\epsilon}_e + \boldsymbol{\epsilon}_p. \tag{46}$$

The Helmholtz free-energy $\psi(\boldsymbol{\epsilon}_e, T, \widehat{\rho})$ is introduced as a function of (i.) the elastic part of the logarithmic strain, (ii.) the temperature T, and (iii.) the inelastic relative density of the material $\widehat{\rho}$, which is the only internal variable introduced in the treatment, defined as

$$\widehat{\rho} = \frac{\rho_0}{\rho_{fd}} e^{-\operatorname{tr}\boldsymbol{\epsilon}_p}, \tag{47}$$

and representing a dimensionless measure of the mass density upon unloading. In Eq. (47) ρ_0 is the initial value of the mass density ρ, and ρ_{fd} the value corresponding to the fully dense material, which contains no pores.

Definition (47) may be better appreciated by writing the rate of mass conservation

$$\frac{\dot{\rho}}{\rho} = -\operatorname{tr}\dot{\boldsymbol{\epsilon}}, \tag{48}$$

which can be integrated in time to provide the expression

$$\log \frac{\rho}{\rho_0} = -\operatorname{tr} \boldsymbol{\epsilon}. \tag{49}$$

From eq. (49) the rate of mass density can be calculated to be

$$\frac{\dot{\rho}}{\rho_{fd}} = [-\widehat{\rho} \operatorname{tr} \dot{\boldsymbol{\epsilon}}_e + (\widehat{\rho})^{\cdot}]\, e^{-\operatorname{tr} \boldsymbol{\epsilon}_e}, \tag{50}$$

where

$$(\widehat{\rho})^{\cdot} = -\widehat{\rho} \operatorname{tr} \dot{\boldsymbol{\epsilon}}_p, \tag{51}$$

an equation which will become useful later.

Note also that the mass density is related to the porosity f (the ratio between the volume of the voids and the total volume of a sample) of the material through the equation

$$\frac{\rho}{\rho_{fd}} = 1 - f. \tag{52}$$

Eq. (52) can be understood considering the deformation gradient $\boldsymbol{F}_{fd}$ and its determinant J_{fd} needed to bring the current volume element V to the volume of the fully dense material V_{fd}. In this deformation, the volume and the density transform according to the well-known rules $V_{fd} = J_{fd} V$ and $\rho = J_{fd} \rho_{fd}$, respectively, so that eq. (52) is obtained, because by definition $f = 1 - V_{fd}/V$.

The so-called elastoplastic coupling (in which the plastic strain influences the elastic stiffness, [2, 21, 57]) is not introduced in the model and the elastic part of the deformation (not particularly important during sintering) will be eventually treated with the standard linear isotropic thermoelastic law [15]. Therefore, the stress $\boldsymbol{\sigma}$, work-conjugate in the Hill sense to the Lagrangian logarithmic strain, the thermodynamical force R associated to the internal variable $\widehat{\rho}$, and the entropy η can be expressed as

$$\boldsymbol{\sigma} = \rho \frac{\partial \psi(\boldsymbol{\epsilon}_e, T, \widehat{\rho})}{\partial \boldsymbol{\epsilon}_e}, \quad R = -\rho \frac{\partial \psi(\boldsymbol{\epsilon}_e, T, \widehat{\rho})}{\partial \widehat{\rho}}, \quad \eta = -\frac{\partial \psi(\boldsymbol{\epsilon}_e, T, \widehat{\rho})}{\partial T}. \tag{53}$$

For simplicity, an additive form of the Helmholtz free energy is assumed, sum of the elastic and the purely thermal energies, plus a 'pore energy'

$$\psi(\boldsymbol{\epsilon}_e, T, \widehat{\rho}) = \psi_e(\boldsymbol{\epsilon_e}, T) + \psi_T(T) + \psi_{pore}(\widehat{\rho}), \tag{54}$$

where

$$\psi_T(T) = -c_h T \log \frac{T}{T_0} + c_h(T - T_0) - \eta_0(T - T_0) + \psi_0, \tag{55}$$

in which T_0 is the absolute temperature corresponding to the unstressed material when $\boldsymbol{\epsilon} = 0$; moreover, η_0 and ψ_0 are the values of entropy η and free energy at $T = T_0$ and $\boldsymbol{\epsilon} = 0$; finally

$$c_h = -T \frac{\partial^2 \psi(\boldsymbol{\epsilon}_e, T, \widehat{\rho})}{\partial T^2}, \tag{56}$$

is the specific heat at constant values of strain and internal variables.

The density, together with the (visco-)plastic strain $\boldsymbol{\epsilon}_p$ are internal variables of the system. The external variables are the total strain $\boldsymbol{\epsilon}$ and the temperature T. To follow the theory of thermodynamics of irreversible processes, the Clausius-Duhem dissipation inequality has to be fulfilled at all times [15, 42], namely

$$-\rho \left(\dot{\psi} + \eta \dot{T} \right) + \boldsymbol{\sigma} \cdot \dot{\boldsymbol{\epsilon}} - \frac{1}{T} \boldsymbol{q} \cdot \nabla T \geq 0. \tag{57}$$

The rate in time of the Helmholtz free energy ψ, eq. (54), can be expressed in terms of its state variables:

$$\dot{\psi} = \frac{\partial \psi_e}{\partial \boldsymbol{\epsilon}_e} \dot{\boldsymbol{\epsilon}}_e + \frac{\partial \psi_T}{\partial T} \dot{T} + \frac{\partial \psi_{pore}}{\partial \widehat{\rho}} (\widehat{\rho})^{\cdot}. \tag{58}$$

The additive decomposition of the strain into an elastic and a (visco-)plastic part, eq.(46), can be inserted into eq.(58) and the

result substituted into eq.(57) to yield

$$
\begin{aligned}
&\underbrace{-\left(\rho\frac{\partial\psi_T}{\partial T}+\rho\eta\right)\dot{T}-\frac{1}{T}\,\boldsymbol{q}\cdot\nabla T}_{\text{thermal dissipation}}+\underbrace{\left(-\rho\frac{\partial\psi_e}{\partial\boldsymbol{\epsilon}_e}+\boldsymbol{\sigma}\right)\cdot\dot{\boldsymbol{\epsilon}}_e}_{\text{elastic dissipation}}\\
&+\underbrace{\left(\rho\,\widehat{\rho}\frac{\partial\psi_{pore}}{\partial\widehat{\rho}}\boldsymbol{I}+\boldsymbol{\sigma}\right)\cdot\dot{\boldsymbol{\epsilon}}_p}_{\text{(visco}-\text{)plastic dissipation}}\geq 0.
\end{aligned}
\tag{59}
$$

Setting the thermal dissipation to be independent of $\dot{T}$ yields equation $(53)_3$, while imposing the vanishing of the elastic dissipation for every $\dot{\boldsymbol{\epsilon}}_e$ in eq. (59) provides equation $(53)_1$, so that using the following simple expression for the potential (borrowed from the linear theory) of the elastic part of the free energy density,

$$
\rho\psi_e=\frac{1}{2}\lambda\left(\operatorname{tr}\boldsymbol{\epsilon_e}\right)^2+\mu\boldsymbol{\epsilon}_e\cdot\boldsymbol{\epsilon}_e-K_b\,\alpha_0\left(T-T_0\right)\operatorname{tr}\boldsymbol{\epsilon}_e,
\tag{60}
$$

the stress is given by the usual isotropic thermoelastic relation

$$
\boldsymbol{\sigma}=\mathbb{C}[\boldsymbol{\epsilon}_e]-K_b\alpha_0\left(T-T_0\right)\boldsymbol{I},
\tag{61}
$$

where K_b is the elastic bulk modulus, α_0 is the thermal expansion coefficient, T_0 a reference temperature, and the fourth-order elasticity tensor $\mathbb{C}$ is

$$
\mathbb{C}=\lambda\,\boldsymbol{I}\otimes\boldsymbol{I}+2\mu\mathbb{S},
\tag{62}
$$

in which $\mathbb{S}$ is the fourth-order symmetrizer and λ and μ are the Lamé elastic moduli.

Eq. (62) represents a strong assumption, which is justified in the present context, because the elastic strain and rotation are usually small during thermoplastic pressing and sintering of ceramics.

As a conclusion, the dissipation inequality eq. (59) reduces to

$$
-\frac{1}{T}\,\boldsymbol{q}\cdot\nabla T+\left(\rho\,\widehat{\rho}\frac{\partial\psi_{pore}}{\partial\widehat{\rho}}\boldsymbol{I}+\boldsymbol{\sigma}\right)\cdot\dot{\boldsymbol{\epsilon}}_p\geq 0.
\tag{63}
$$

3.1 Effective stress for sintering and dissipation

An inspection of eq. (63) and consideration of eq. $(53)_2$ reveals that the thermodynamic dual force to the plastic strain rate is not the stress, but an effective stress defined as [20, 41]

$$\hat{\boldsymbol{\sigma}} = \boldsymbol{\sigma} - \sigma_s \boldsymbol{I}, \tag{64}$$

where

$$\sigma_s = \widehat{\rho} R = -\widehat{\rho}\rho \frac{\partial \psi}{\partial \widehat{\rho}} \tag{65}$$

is the so-called 'sintering stress' (also known as 'Laplace pressure' [22]). Eventually, the dissipation inequality, eq. (63), can be rewritten as

$$-\frac{1}{T}\boldsymbol{q} \cdot \nabla T + \hat{\boldsymbol{\sigma}} \cdot \dot{\boldsymbol{\epsilon}}_p \geq 0, \tag{66}$$

which highlights the fact that the inequality is always a-priori satisfied, when the Fourier law of heat conduction is assumed

$$\boldsymbol{q} = -k \nabla T, \tag{67}$$

(in which $k > 0$ is the thermal conductivity), together with the normality rule for $\dot{\boldsymbol{\epsilon}}_p$ and convexity of the yield function, both in the $\hat{\boldsymbol{\sigma}}$-space.

3.2 Helmholtz free energy for porosity variation

Following [41], the Helmholtz free energy related to the porosity, ψ_{pore}, can be assumed to be a linear function of the surface tension γ_s relative to the area of the pore $A_{pore}(\widehat{\rho})$ as follows

$$\psi_{pore} = \frac{\gamma_s A_{pore}(\widehat{\rho})}{\rho V} = \frac{\gamma_s A_{pore}(\widehat{\rho})}{\rho_{fd} V_{solid}}. \tag{68}$$

Assuming spherical pores of radius r in a cubic unit cell, it follows that $A_{pore} = 4\pi r^2$ and assuming incompressibility of the solid phase of volume V_{solid}, r can be expressed as

$$r = \left(V_{solid} \frac{3(1-\widehat{\rho})}{4\pi\widehat{\rho}} \right)^{1/3}, \tag{69}$$

so that the pore potential, eq. (68), becomes

$$\psi_{pore} = \frac{\gamma_s}{\rho_{fd} V_{solid}^{1/3}} 4\pi \left(\frac{3(1-\widehat{\rho})}{4\pi\widehat{\rho}} \right)^{2/3}. \tag{70}$$

Finally, a derivative of eq. (70) with respect to $\widehat{\rho}$ yields the sintering stress as

$$\sigma_s = \underbrace{\frac{8\pi}{3} \left(\frac{3}{4\pi} \right)^{\frac{2}{3}}}_{\approx 3.224} \frac{\gamma_s}{V_{solid}^{1/3}} \left(\frac{\widehat{\rho}}{1-\widehat{\rho}} \right)^{1/3}, \tag{71}$$

where $V_{solid}^{1/3}$ can be regarded as a length scale, equal to the particle diameter.

4 Visco-Plasticity

The existence of a yield function is assumed. This function depends on the effective stress $\hat{\boldsymbol{\sigma}}$, which is the thermodynamic dual of the plastic strain rate, and on the internal variable $\widehat{\rho}$

$$\mathcal{F} = \mathcal{F}(\hat{\boldsymbol{\sigma}}, \widehat{\rho}, T). \tag{72}$$

The associative flow rule is assumed [15, 40] involving the non-negative plastic multiplier $\dot{\lambda}$

$$\dot{\boldsymbol{\epsilon}}^p = \dot{\lambda} \boldsymbol{Q}, \tag{73}$$

where the unit yield function gradient is

$$\boldsymbol{Q} = \frac{\frac{\partial \mathcal{F}(\hat{\boldsymbol{\sigma}}, \widehat{\rho}, T)}{\partial \hat{\boldsymbol{\sigma}}}}{\left\| \frac{\partial \mathcal{F}(\hat{\boldsymbol{\sigma}}, \widehat{\rho}, T)}{\partial \hat{\boldsymbol{\sigma}}} \right\|}. \tag{74}$$

For rate-dependent problems the coefficient $\dot{\lambda}$ can be replaced with an overstress function, as described in [47]. A possible choice for the overstress function is the yield function divided by the viscosity (η_v). The expression for the strain rate becomes:

$$\dot{\boldsymbol{\epsilon}}^p = \frac{1}{\eta_v} \langle \mathcal{F} \rangle \boldsymbol{Q}. \tag{75}$$

4.1 Yield Function

The Bigoni-Piccolroaz yield function [7] is defined by seven parameters and displays the necessary flexibility to describe a wide range of material behaviors and, in particular, can excellently fit the material behavior during the different states of sintering. The material undergoes a large variety of states from the beginning as a fluid-like powder, to the intermediate state as a plastic body, up to the end state as a brittle solid. This is why the large flexibility of the function is needed to describe the full range of

the process. Therefore, the sintering process can be simulated from the beginning, when the material is in a granular form, and then during the firing up to the finished ceramic piece. The yield function is described by

$$\mathcal{F}(\boldsymbol{\sigma}, M, p_c, c, \alpha_{bp}, \Theta_c, \gamma_{bp}, \beta_{bp}) = F(p, M, p_c, c, \alpha_{bp}) + q\, g(\Theta_c, \gamma_{bp}, \beta_{bp}), \tag{76}$$

where

$$p = -\operatorname{tr}\boldsymbol{\sigma}/3 \qquad q = \sqrt{\frac{3}{2}\operatorname{dev}(\boldsymbol{\sigma}) \cdot \operatorname{dev}(\boldsymbol{\sigma})} \tag{77}$$

(dev denotes the deviator part) and

$$\begin{aligned} F(p, M, p_c, c, \alpha_{bp}) &= -M p_c \sqrt{[\Phi_{bp} - (\Phi_{bp})^m][2(1-\alpha_{bp})\Phi_{bp} + \alpha_{bp}]}, \\ \Phi_{bp} &= \frac{p + c}{p_c + c}, \\ g(\Theta_c, \beta_{bp}, \gamma_{bp}) &= \cos\left[\beta_{bp}\frac{\pi}{6} - \frac{1}{3}\cos^{-1}(\gamma_{bp} cos(3\Theta_c))\right], \end{aligned} \tag{78}$$

in which the Lode angle Θ_c is defined as

$$\Theta_c = \frac{1}{3}\cos^{-1}\left(\frac{9\ \operatorname{tr}(\operatorname{dev}\boldsymbol{\sigma})^3}{2\, q^3}\right). \tag{79}$$

Parameters α_{bp} and m can be used to adjust the yield function to materials with internal friction. Parameters β_{bp} and γ_{bp} determine the shape of the yield surface in the deviatoric plane, so that for both simplicity and lack of experimental data they are set to be zero, which means that Lode angle dependence is excluded (note that for triaxial compression the Lode angle Θ_c is equal to $\pi/3$, while it is zero for triaxial extension). The cohesion c is the hydrostatic yield strength in extension whereas p_c is the yield strength in hydrostatic compression.

5 Alumina Experiments

5.1 Uniaxial compression tests

A pilot experimental study was performed to study the yield points of partially sintered ceramics.
In order to model the plastic behavior of the material it is essential to know the point at which the the material plastically deforms, the yield stress.
For this study, cylindrical specimen were pressed, to a density of about 60 % with a pressure of 60MPa.
These specimens were sintered at different isothermal temperatures for one hour.
A higher sintering temperature results in a denser compact and so the specimen have different relative densities.
The sintered specimen were tested with a universal testing machine under uniaxial compression. The setup is shown in figure 3. The testing was performed on a machine from Messphysik, in the solid mechanics laboratory of the University of Trento.
It was found that the strength increase is very steep for the beginning of the sintering at which the relative density changes just slightly.
Thus, it can be assumed that other factors than just the density determine the strength.

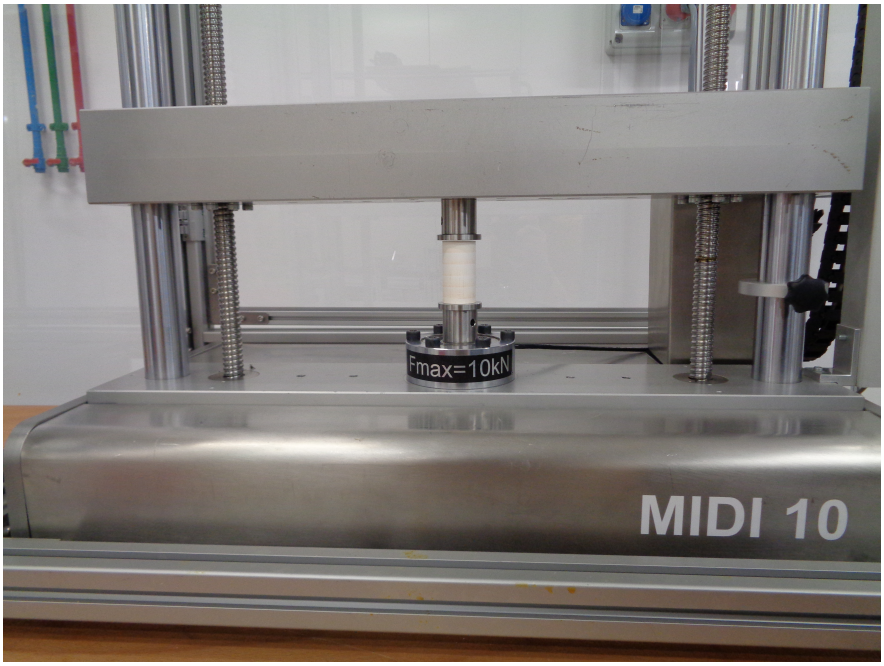

Figure 3: The machine setup for the pre study. A Messphysik Midi 10 Universal Testing Machine.

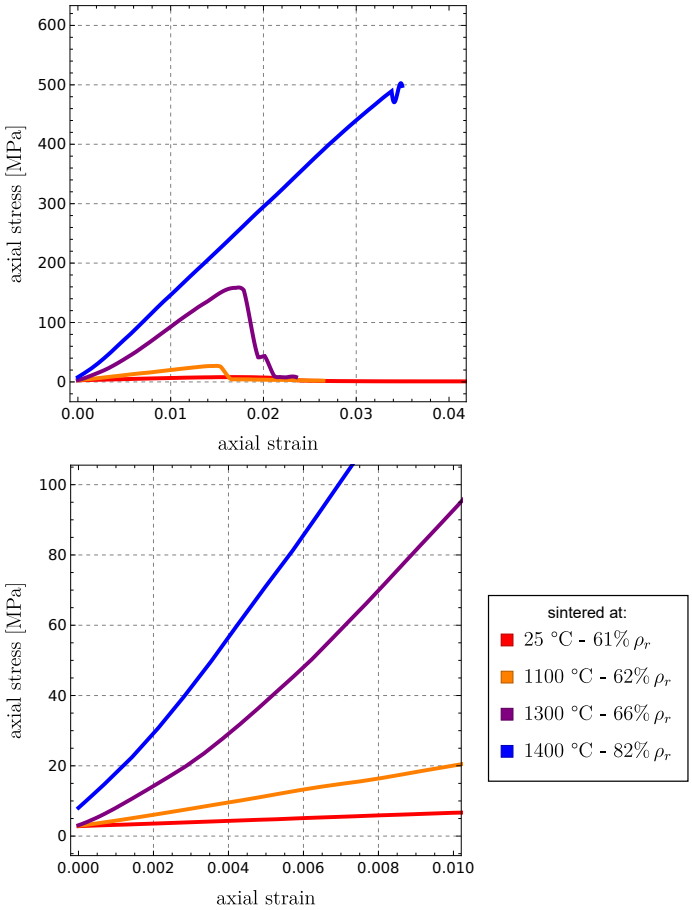

Figure 4: The results of the pre study which shows the steep increase of stiffness and yield strength for the beginning of sintering. Both graphs show the same results, the upper one shows the overall results in one plot, the lower graph shows an extract in bigger detail.

Figure 5: The cylindrical specimen for the study. The height is about 58mm and the width about 30mm.

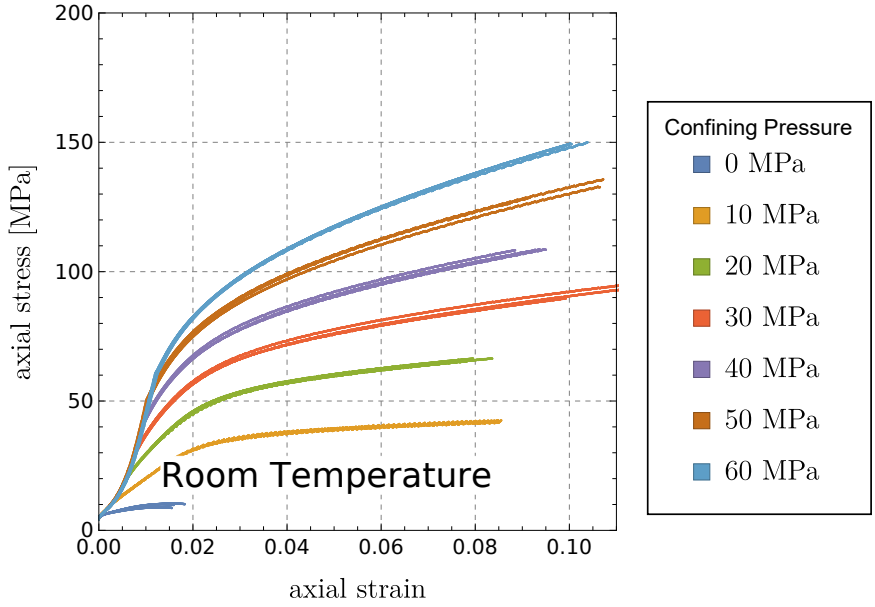

Figure 6: The stress strain curves for all the performed tests on the specimen that were unsintered..

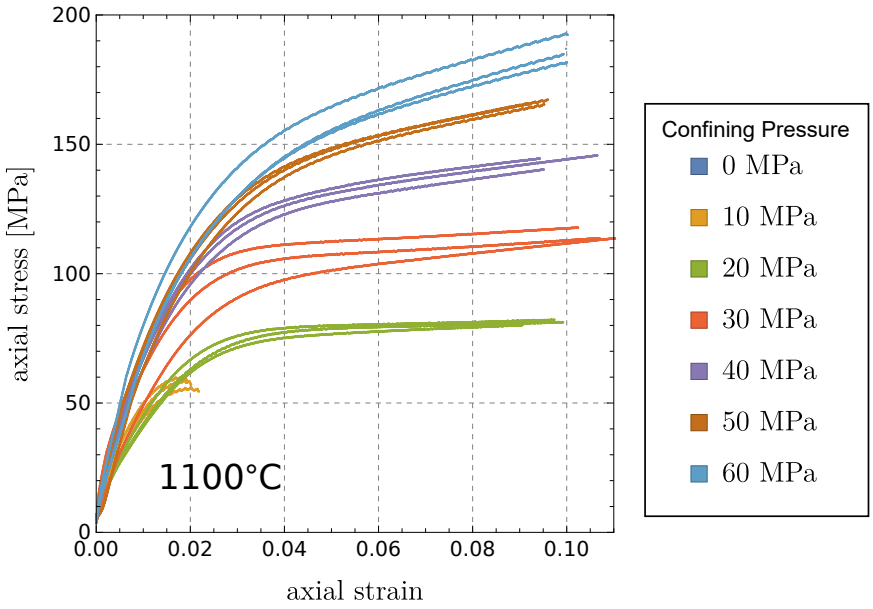

Figure 7: The stress strain curves for all the performed tests on the specimen that were sintered at 1100 Degress Celsius

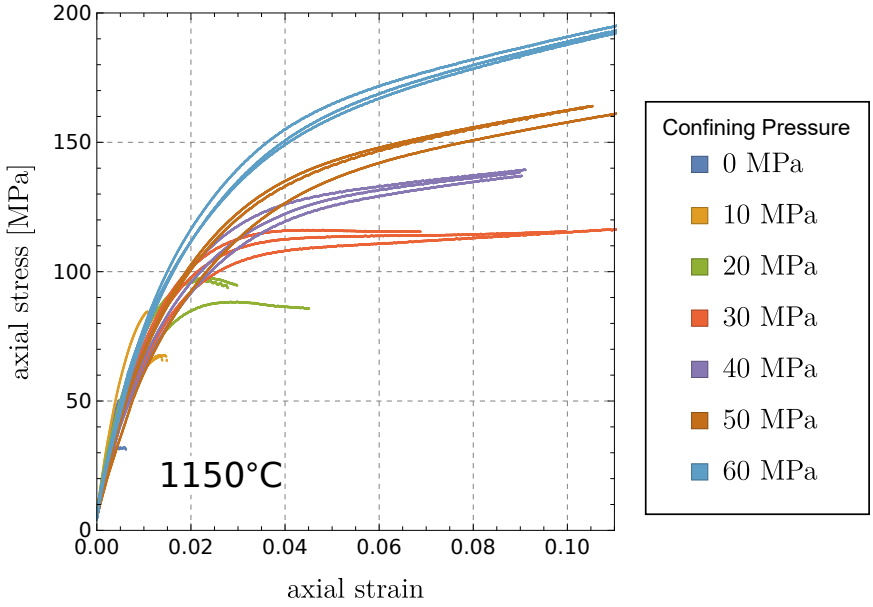

Figure 8: The stress strain curves for all the performed tests on the specimen that were sintered at 1150 Degress Celsius

5.2 Triaxial tests

For the triaxial Tests, the specimen were manufactured in the same way as for the pre study. The specimen were subjected to two different sintering temperatures and one comparative study was performed on the green bodies. The bodies were heated up with $3°C/min$ and then held at isothermal temperature of $1100°C$ and $115°C$ for one hour.

The test results are depicted in figures 10-12. From the fitted curves it can be seen, that we can achieve a fairly good fit by changing only the parameters M, pc and c, which assumes isotropy.

Figure 9: The machine setup for the triaxial Tests. An Instron 600DX Universal Testing Machine coupled with a Hoek Triaxial Cell (600bar)

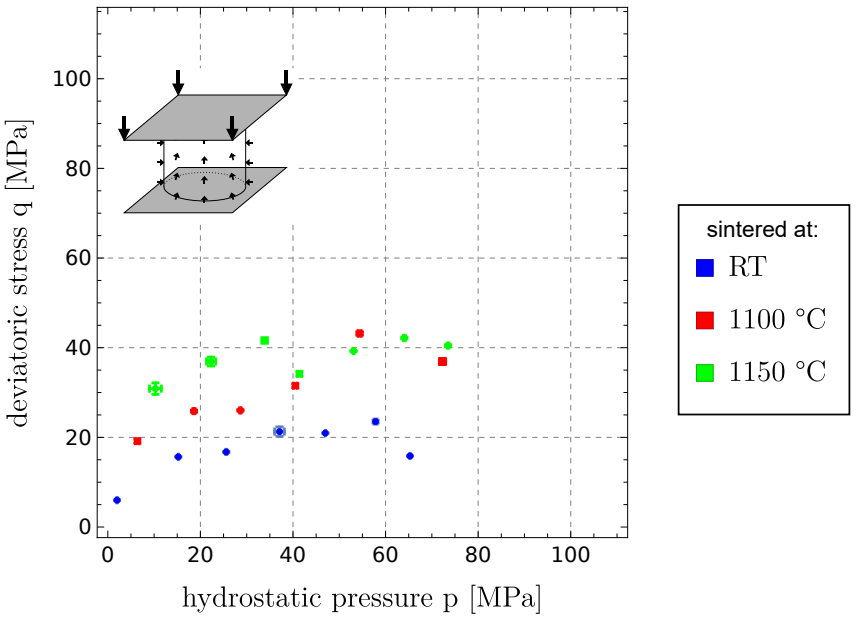

Figure 10: The results of the performed experiments. Each point depicts the ultimate limit of the test, while the error bars show the variation within the same type of test.

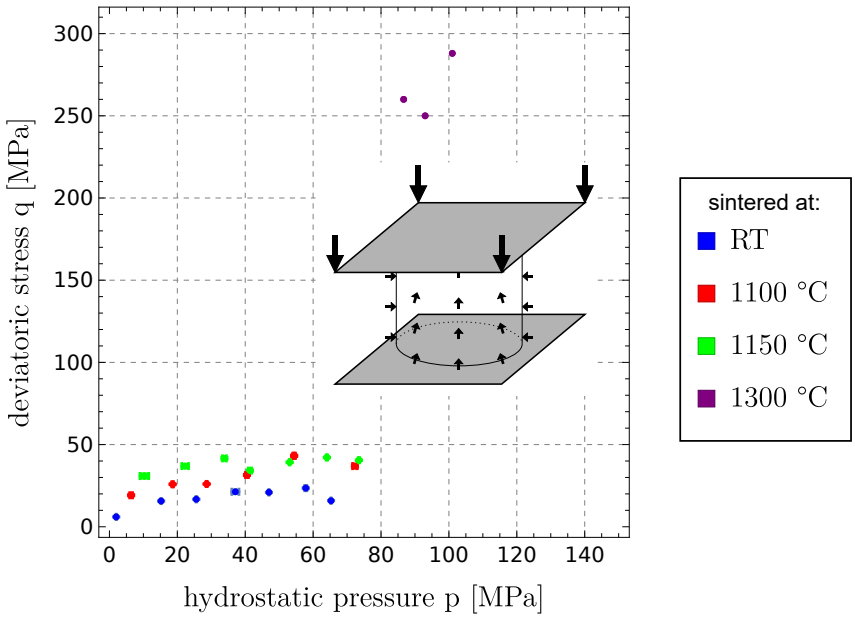

Figure 11: The results of the performed experiments. Each point depicts the elastic limit of the test, while the error bars show the variation within the same type of test. As can be seen just a few percent increase in density increases the strength dramatically.

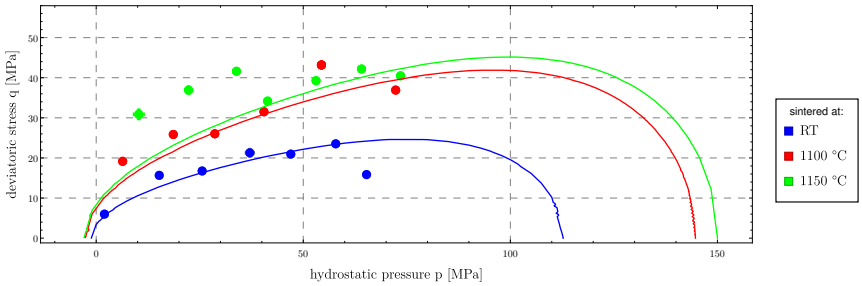

Figure 12: The results of the performed experiments. The curves display the fit of the Bigoni-Piccolroaz yield surface through the experimental values. The fitting has been done with a least-squares type of fit using Mathematica 11.

5.3 Conclusion of the preliminary experimental study

The experiments with alumina material have shown, that in general, it is possible to fit the Bigoni-Piccolroaz yield function to experimentally obtained values for ceramic material (see Figure 12). However, the range of densities that can be considered is very small. The main reason is that with standard triaxial test machines, the applicable confining pressures are too low. Another problem is that triaxial tests with standard apparatus cannot be conducted at high temperatures, becasue the pressures are applied with hydraulic oil, which is flammable. It is therefore necessary, to apply other means. In the next chapter, a micromechanical model is introduced to circumvent the need for triaxial experimental values.

6 Micromechanics for the evolution of yield

To model the compaction behavior of a green body during the sintering process, the following micromechanic assumptions are introduced, which allows for the determination of the hardening parameters p_c, c, and M (dictating the shape of the yield function), as functions of the internal variable $\widehat{\rho}$. It should be noted that the determination of the evolution of parameter p_c with the inelastic density $\widehat{\rho}$ is equivalent to the determination of the theoretical compaction curve for a granulate material. This material is assumed to consist of elastic perfectly plastic particles, idealized as cylinders in a two-dimensional approximation and obeying the Tresca yield criterion, that are equal in size and ordered in a centered cubic geometry, a disposition maintained fixed during sintering. The results of the two-dimensional approach is then tested against numerical simulations for a cubic disposition of perfectly-plastic spherical particles, obeying the von Mises criterion. The particles thus yield all simultaneously. In oder to predict the collapse load for this ensemble of particles it is then possible to use a limit analysis technique (see [11]).

6.1 Plane strain upper bound for the determination of the compaction curve

A plane strain problem is considered, so that the particles are assumed in the form of circular cylinders, a geometry which may seem unrealistic, but has been proven to yield quite reasonable results [2, 18]. Employing the upper bound theorem [11], a collapse mechanism has to be assumed, which, even if it does not correspond to reality, provides a simple evaluation of the dissipation that occurs within the body. Because the problem is reduced to two-dimensions, the particles are treated as planar figures, initially circular and later deforming and developing con-

tacts through lines.

A collapse kinematics is assumed, in which rigid parts are subject to a pure rigid-body translation, while deformable parts are subject to a pure compressive strain, so that the latter (denoted by $|\epsilon|$ in Figure 13) are located on the surface of the particle in contact with the neighboring particles and the former are localized at the circular corners. The plastic mechanism has two axes of symmetry (vertical and horizontal) so that only a quarter of the particle is sketched and the two deformational parts suffer the same strain and dissipate the same power.

The plastic dissipation is generated by the strain rate produced under uniaxial stress in two equally deforming blocks (denoted by $|\epsilon|$ in Figure 13) and their sliding against a square rigid block located at the center of the particle and other two rigid block with the shape of a quarter of circle.

For an equibiaxial (vertical and horizontal) compression load P, which simulates mechanical compaction, the 'external' rate of energy dissipation $\dot{W}$ can be written as

$$\dot{W} = 2Pv_b, \tag{80}$$

where v_b is the velocity of the boundary in contact with the neighboring particles.

The rate of internal power (denoted by D) is the sum of three dissipation sources, D_{comp}, D_{slb}, and D_{tr}, all related to the deformation of the blocks denoted with with the label $|\epsilon|$ in Figure 13. These blocks are subject to a linear velocity field preserving incompressibility, so that, assuming a x_1-x_2 reference system, with x_2 parallel to v_b

$$v_1 = \frac{v_l}{a}x_1, \quad v_2 = \frac{v_b}{h}x_2, \tag{81}$$

where incompressibility requires $v_b a = -v_l h$. Therefore, the three sources of dissipation rate can be calculated as follows.

- Internal dissipation due to the strain rate of the rectangular

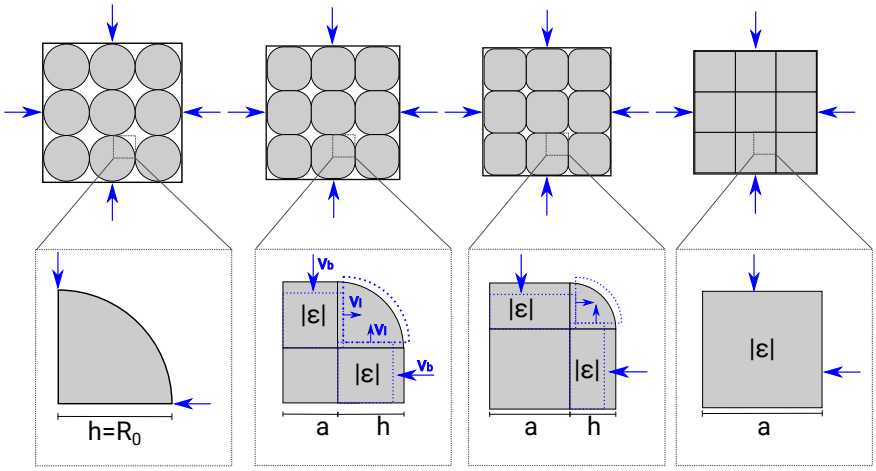

Figure 13: Assuming that the granules behave as rigid-perfectly-plastic materials, the isostatic compaction curve can be calculated using the upper bound technique of limit analysis. A representative volume element of an idealized 2D granular arrangement is shown in the figure at various stages of the compaction. As the borders of the RVE are displaced with the velocities v_b, the RVE shrinks. A section view of the assumed collapse mechanism for a fourth part of the circular particle, is reported in the lower line, where the dashed lines sketch the particle boundaries subject to a displacement rate.

blocks $|\epsilon|$

$$D_{comp} = 4kv_b a, \tag{82}$$

where k is the limit yield under shear (equal to $1/2$ of the limit stress under uniaxial stress).

- Dissipation due to the sliding of the blocks $|\epsilon|$ against the rigid square block at the center of the particle and against the quarter of circle rigid element

$$D_{slb} = 2k\left(\int_0^a v_l\, s\, ds + \int_0^h v_b\, s\, ds\right) = v_l ak + v_b hk. \tag{83}$$

- Dissipation due to rigid translation of the quarter of circle rigid element with sliding against one of the blocks $|\epsilon|$

$$D_{tr} = 2v_l hk, \tag{84}$$

so that the internal expended power can be written as

$$D = kv_b\left(6a + a^2/h + h\right). \tag{85}$$

Eventually the limit load P can be expressed as a function of the current geometry as

$$P = k\left(3a + \frac{1}{2}\frac{a^2}{h} + \frac{1}{2}h\right), \tag{86}$$

corresponding to the limit pressure that the particle characterized by the dimensions a and h can sustain.

The width of the compressed part a and its height h can be expressed as functions of the relative density and the current radius R of the unit cell, so that, keeping into account incompressibility, the following expression is found

$$\begin{aligned}\widehat{\rho} = \frac{A_0}{A_{UC}} &= \frac{2ha + a^2 + \frac{1}{4}\pi h^2}{R^2} \\ &= \frac{2h(R-h) + (R-a)^2 + \frac{1}{4}\pi h^2}{R^2},\end{aligned} \tag{87}$$

where A_{UC} denotes the area of the unit cell containing the particle of area A_0. An expression for R can also be found using the incompressibility, and thus the fact that the initial area of the two-dimensional particle remains constant:

$$\widehat{\rho} = \frac{\frac{1}{4}\pi R_0^2}{R^2}, \quad \Rightarrow \quad R = \frac{R_0}{2}\sqrt{\frac{\pi}{\widehat{\rho}}}. \tag{88}$$

Equation (87) can be solved for h, so that using eq. (88) yields

$$h = \sqrt{\frac{\pi R_0^2(1-\widehat{\rho})}{\widehat{\rho}(4-\pi)}} \tag{89}$$

and therefore the contact length a results as

$$a = R - h. \tag{90}$$

The hydrostatic yield stress p_c is given by the force per unit length P divided by R, so that the following representation of the compaction curve is obtained:

$$p_c = k\frac{\sqrt{\pi}\left(-8 + (12 + \pi - 16\widehat{\rho})\sqrt{\frac{\widehat{\rho}-1}{\pi-4}} + 8\widehat{\rho}\right)}{8\widehat{\rho}(\widehat{\rho}-1)} \tag{91}$$

Eq. (91) describing the compaction curve of a granular material is depicted in Figure 15.

Formally, Eq. (91) merely represents an upper bounds calculated for a plane strain situation, which may be believed to be far from reality, so that an assessment of the compaction curve is provided through comparison to a Finite Element simulation involving a three-dimensional distribution of spherical particles. The simulation was performed with initially perfectly-plastic spherical particles, ordered in a simple cubic geometry. Initially the contact is through a point, but due to the deformation the contact boundary becomes circular. This periodic particle arrangement can be modelled using only an eighths of a sphere, due to

symmetry. A FEM model was built in Abaqus 6.13, where displacement was imposed through analytical rigid body elements, sketched as colored planes in Figure 14, where a unit cell containing a deformed particle is shown. The material obeys von Mises plasticity, together with a neo-Hookean description for the elastic part, with high stiffness of 100000 MPa, to approximate the rigid-plastic limit. It can be seen that for lower densities (about 0.8 and less) the solution of the limit analysis is remarkably different from the numerical solution of the 3D problem, which is a direct consequence of the fact that the initial density for the 2D problem is different than that pertinent to the 3D arrangement. In fact the relative density in plane strain is about 78%, while this density decreases to about 52%, when all particles are spherical. Moreover, the density of a typical ceramic powder (as that later used for experiments, section 8.5) has an initial density of about 38%. A very simple way for correcting the discrepancy between the plane strain upper buond estimate and the values typical of ceramic powders is to introduce a correction factor ζ multiplying h, so that the initial value of p_c becomes correct even for initial densities of 38% and therefore

$$h_{mod} = \zeta \, R_0 \sqrt{\frac{\pi(1-\widehat{\rho})}{\widehat{\rho}(4-\pi)}}, \tag{92}$$

where $\zeta = 2.7$ will provide the best fit to the material considered in the experiments. A substitution of eq. (92) into eq. (80) yields an analytical expression the compaction behaviour

$$p_c(\widehat{\rho}, \sigma_m) = \sigma_m \frac{-530 + (619 + 25\pi - 719\widehat{\rho})\sqrt{\frac{\widehat{\rho}-1}{\pi-4}} + 530\widehat{\rho}}{210\sqrt{3}(\widehat{\rho}-1)}. \tag{93}$$

where $\sigma_m = k\sqrt{3}$ is the uniaxial stress for yielding. Note that eq. (93) provides an analytical description for the compaction curve of a granulate, which will be referred as the 'modified limit analysis solution'.

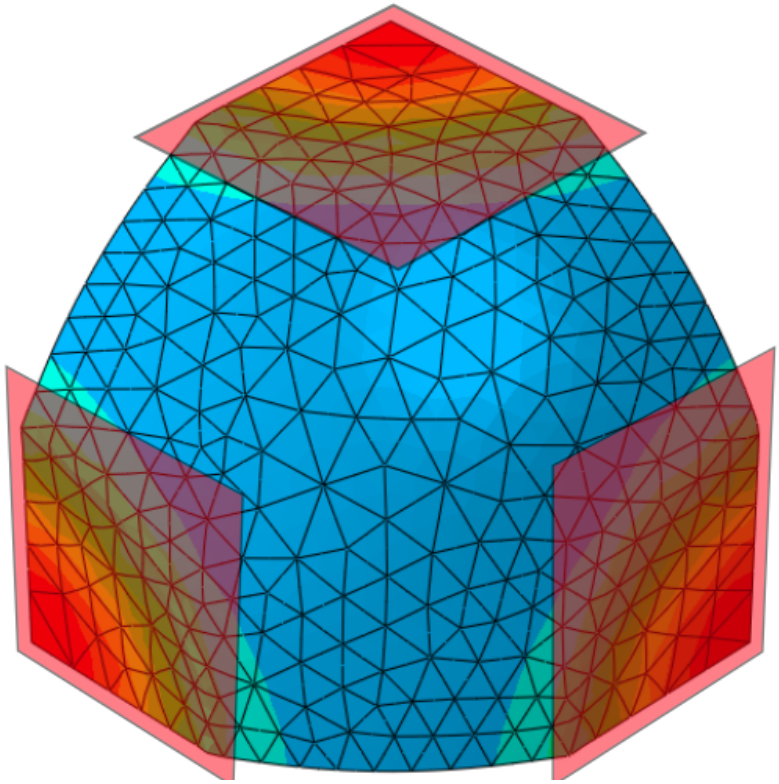

Figure 14: The FEM model of the particle. An initially spherical particle is pressed into a cubic shape by three analytical contact surfaces (shown as translucent red surfaces) that move towards the center of the cell, with imposed displacements. Incompressible hybrid elements are used together with neo-Hookean material model for the elastic part, while the plastic behavior is modelled with von-Mises perfect plasticity.

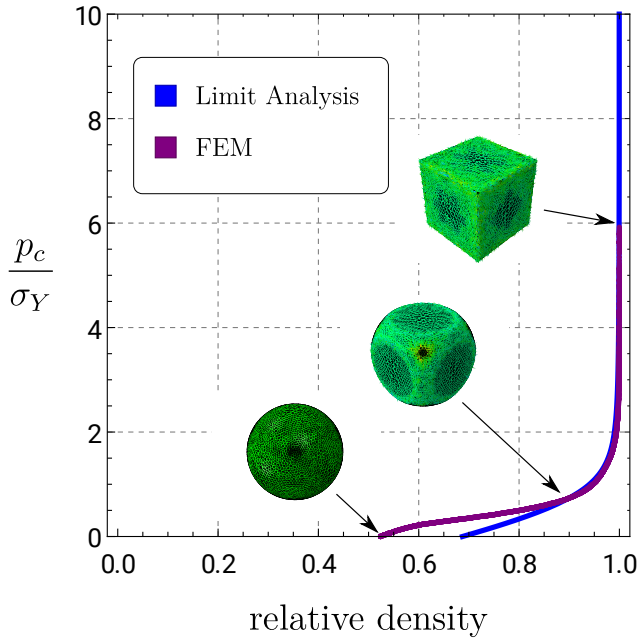

Figure 15: Comparison between the analytical results obtained with a two-dimensional application of the upper bound theorem of limit analysis and a three-dimensional FE simulation of the unit cell shown in Figure 14.

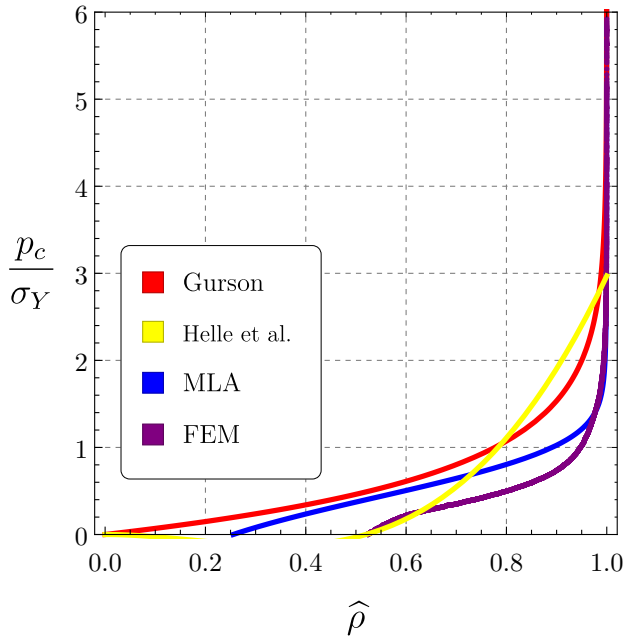

Figure 16: Comparison of the Gurson ([26]) and Helle/Fleck ([18, 28]) models with the upper bound analytical solution, eq. (93), and the three-dimensional FE simulation of the unit cell shown in Figure 14.

A comparison is presented in Figure 16 of the Gurson [26] and Helle/Fleck [18, 28] models with the previously-described FE simulation of a three-dimensional unit cell (see Fig. 14). The modified limit analysis solution for the 2D model is also included and it can be noted that this solution lies below the curves corresponding to the Gurson and Helle/Fleck models, at high porosity. It needs to be mentioned that the Gurson model was originally developed for materials with high porosity, where there is a nice comparison with the modified upper bound solution and the numerical simulation, whereas the model presented by Helle [28] (and used also by Fleck [18]) was intended for cases of low porosities, where, again, a good fit is found with the modified upper bound and the numerical simulation.

6.2 Cohesive strength under tension

The values for p_c (under compressive load) have been determined as a function of the relative density. The cohesion strength c can be evaluated as a function of the internal variable $\widehat{\rho}$ from the following simple micromechanical model. Simulations performed with the unit cell sketched in a deformed state in Fig. 14 show that the contact area between initially spherical grains in a cubic geometry is a complex function of the applied pressure, so that an initially circular contact area evolves towards a square contact shape. Therefore, the estimation of the contact areas between grains in a real powder distribution is awkward. Nevertheless, following [28], the following approximation for the contact area A_c between grains is

$$A_c = \frac{4\pi}{12} \frac{\widehat{\rho} - \widehat{\rho}_0}{1 - \widehat{\rho}_0}, \tag{94}$$

so that the stress needed to produce yielding under hydrostatic tension (which is the definition of the cohesion c) is given by the elementary formula

$$c = \sigma_m \, A_c, \tag{95}$$

where σ_m is the yielding stress in uniaxial tension of the grains.

6.3 Strength under shear for the determination of parameter M

Using again relation (94), the parameter M can be expressed as a function of the internal variable $\widehat{\rho}$. In particular, it is assumed that at failure under pure shear ($p = 0$ so that $\boldsymbol{\sigma} = \operatorname{dev}\boldsymbol{\sigma}$) the deviatoric component of the stress tensor becomes, according to the von Mises criterion, $\frac{\sigma_m}{3}A_c$, so that the stress invariant q at failure (denoted by q_s) reduces to $\sigma_m A_c$. Assuming additionally $\beta = \gamma = 0$ one can resolve the main equation of the BP yield function eq. (78) to obtain an expression for the parameter M:

$$M = \frac{\sqrt{3}\sigma_m A_c}{p_c\, 2\sqrt{[\frac{c}{p_c+c} - (\frac{c}{p_c+c})^m][2(1-\alpha_{bp})(\frac{c}{p_c+c}) + \alpha_{bp}]}}. \tag{96}$$

6.3.1 Simplified Contact Area

The real particle shape during compression is relatively complex. It can be simplified by assuming a particle that is symmetric with respect to the three principal planes, and has quadratic contact surfaces, as shown in Figure 17. Due to the symmetry it is enough to regard an eight of the particle, and we denote the height of the bounding box with R, the side length of the contact surface with a. The contact surface A_c is then simply:

$$A_c = a^2. \tag{97}$$

The side length a is a function of the relative density. The function can be found by assuming incompressibility of the particle, then the volume of the particle V_p is constant while the relative density is given by the Volume of the particle divided by the volume of the unit cell:

$$\rho_{rel} = \frac{V_p}{R^3}. \tag{98}$$

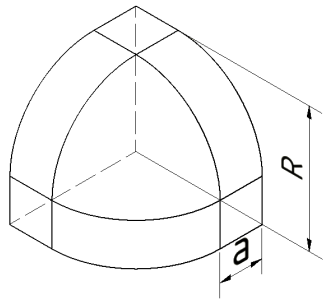

Figure 17: An eight part of the symmetric simplified particle shape

The volume of the particle is constant and equal to $\frac{\pi}{6}R_0^3$ but can also be expressed as:

$$V_p = a^3 + 3ha^2 + \frac{3}{4}\pi ha + \frac{1}{8}\frac{4}{3}\pi h^3 = \frac{\pi}{6}R_0^3, \tag{99}$$

where h is given by:

$$h = R - a. \tag{100}$$

It is now possible to solve eq. (99) for a. This can be inserted into eq. (97) to yield an expression for the contact area.

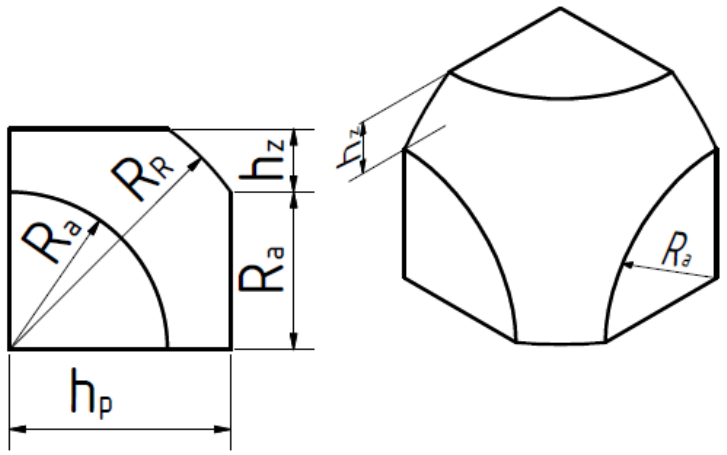

Figure 18: An eight part of the symmetric simplified particle shape, assuming a spherical particle with the tops cut off, leaving circular contact surfaces.

6.3.2 Three dimensional upper and lower bounds for circular contacts

Assuming a simplified particle shape as shown in Figure 18, it is possible to derive upper bounds for a three-dimensional structure. As we assume incompressibility the volume of the particle is constant for the whole process. The density can be given at any moment by dividing the volume of the particle through the volume of the bounding box:

$$\rho_{rel} = \frac{1}{8}\left(\frac{\frac{4}{3}\pi R_{R0}^3}{h_p^2}\right), \tag{101}$$

with R_{R0} being the initial radius of the particle. It is assumed that the particles are initially perfectly spherical thus the initial relative density is $\rho_{rel} = \pi/6$. As the particle will be compacted more and more, the contact surfaces come closer to each other

and will touch, when R_a is equal to h_p. At this point the relative density is $\rho_{rel} = \frac{5\pi}{16} \approx 0.981$.

To compute the upper bound for this span of densities, a collapse mechanism has to be assumed. The mechanism consists of cylindrical bodies that are compressed.This process creates dissipaption in a number of ways. The pure compression denoted by D_{pc}. The contact surfaces move to the center of the particle at collapse. Due to the incompressibility of the material, the cylinder shrinks in height but grows in radius. Due to this the material outside of the cylinders is pushed away. It is assumed that this part of the particle remains rigid and thus creates dissipation through sliding along its surfaces. Each of the cylinders is loaded with the maximum unidirectional tension possible, which is $2k$ for the Tresca criterion. In the middle of the particle the cylinders intersect and create a part that is under hydrostatic tension. This intersection can be described by a Steinmetz body. Hydrostatic loading does not create any dissipation. Therefore, each cylinder just dissipaptes energy for its volume outside of the hydrostatic field. As the geometry is very difficult, at this point we assume a simplified geometry, where the cylinders are at which the dissipating volume of each cylinder is assumed to be $\frac{\pi R_a^2}{4} h$.

$$D = D_{sg} + D_{cz} + D_{sbc} + D_{sbt} + D_{cr} = 3PV_0 \tag{102}$$

$$D_{sg} = 3k \int v_E \frac{r}{R_a} dA = 3k \int_0^{R_a} \int_0^{\pi/2} v_E \frac{r}{R_a} d\phi dr, \tag{103}$$

where v_E is the velocity of the cylindrical surface in radial direction.

$$v_E = \frac{V_0 R_a}{2a}, \tag{104}$$

insertion of eq. (104) into eq. (103) yields

$$D_{sg} = 3k \frac{\pi R_a^3 V_0}{4h} \tag{105}$$

The Dissipation D_{cz} is due to the compression of the cylindrical parts and is given by $2k$ times the volume times the dissipation rate:

$$D_{cz} = 3 \cdot 2k \, \frac{\pi R_a^2}{4} \, h \, \frac{1V_0}{2h} = \frac{3}{4} k \pi R_a^2 V_0. \tag{106}$$

The compressed cylinders slide with their bottom surface over the hydrostatic cube in the middle of the particle. The dissipation for this mechanism is denoted D_{sbc} and given by the the mean of the velocity over the surface times the surface multiplied with k (the shear strength):

$$D_{sbc} = 3 \cdot k \, \frac{2\pi R_a h}{4} \frac{1V0}{2} = 3k \frac{\pi R_a h V_0}{4}. \tag{107}$$

Additionally the material outside of the compressed regions is assumed to translate as a rigid body away from the center in the direction of $\{1, 1, 1\}$. It thus produces a sliding dissipaption between the cylinders and the rigid body which is denoted by D_{sbt}:

$$D_{sbt} = 3 \cdot k \, \frac{2\pi R_a h}{4} v_E = 3 \cdot k \, \frac{\pi R_a^2 V_0}{4}. \tag{108}$$

The last part of the dissipation is created by a separation of surfaces between the rigid body part and the surface of the hydrostatic cube in the middle of the particle the dissipation D_{cr} is given by the separation velocity times the surface times k:

$$D_{cr} = 3 \cdot k \left(R_a^2 - \frac{3}{4} \pi R_a^2 \right) V_E = 3k R_a^3 \left(1 - \frac{3}{4} \pi \right) \frac{V_0}{2h}. \tag{109}$$

Inserting everything in eq. (102) yields

$$P = k \left(\frac{\pi R_a^3}{4h} + \frac{1}{2} \pi R_a^2 + \frac{1}{4} \pi R_a h + \frac{1}{2h} R_a^3 (1 - \frac{1}{4} \pi) \right) \tag{110}$$

This equation can be solved for P by inserting eq. (98) - (100). But the solution includes a complicated relationship that cannot

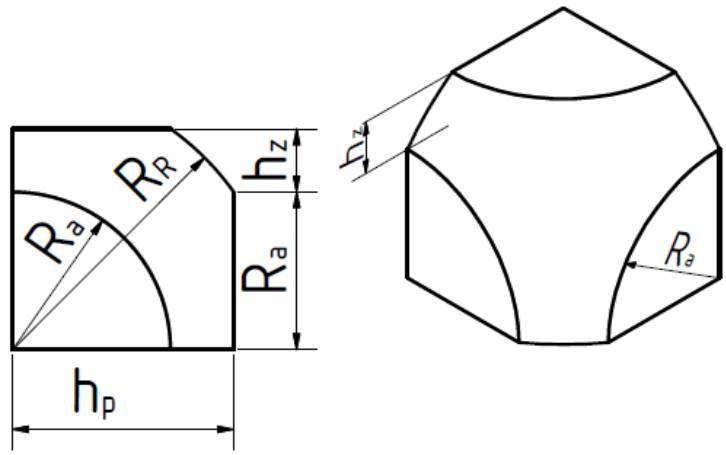

Figure 19: The internal structure of the collapse mechanism sketched.

be solved explicitely in a straight-forward way. The solution can be calculated easily by using a a computational software, such as Mathematica, and the result is shown in Figure 21. For the rest of this work, the formula derived by the 2D method will be used, as it is a relatively easy explicit formula that can be implemented easily into an FEM code.

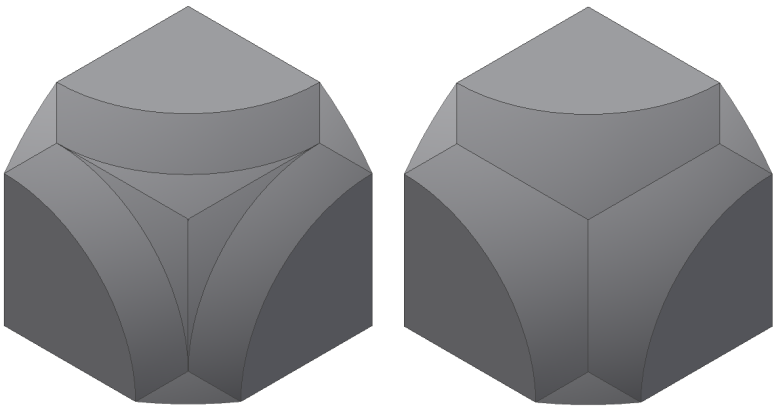

Figure 20: The internal structure of the collapse mechanism is shown. The part that is nod under compression, but moves by rigid body sliding mechanism is made transparent. The left one is the modified collapse mechanism, whereas the right side shows the junction of three perfect cylinders, which was the originally assumed mechanism.

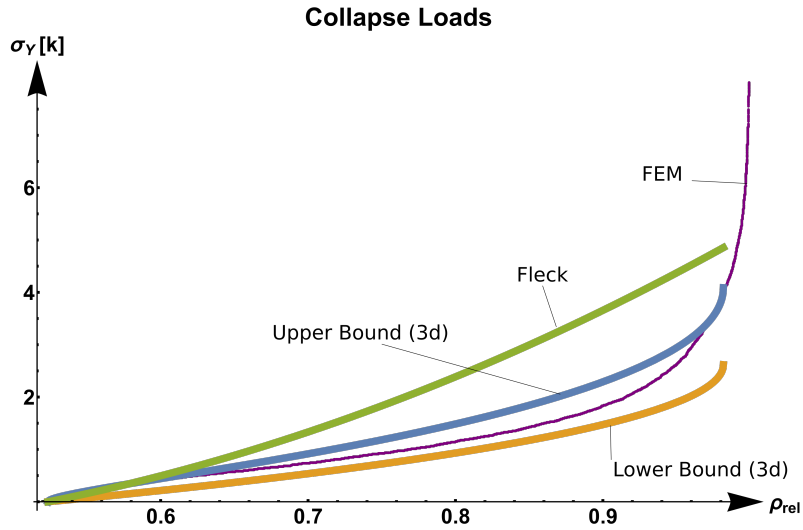

Figure 21: The plot shows the upper and lower bound for the 3D model with circular contact surfaces in comparison with an FEM simulation and the model of Fleck/Helle [18, 28].

7 Influence of Temperature

The consolidation process of a ceramic body is activated at high temperatures, where the material exhibits a strong thermal softening. Also, the viscosity changes drastically with temperature, so that viscoplastic processes occur at much higher velocities at high temperatures.

7.1 Temperature evolution

In the framework proposed by Simo and Miehe [55], the temperature evolution is governed by the Fourier law of heat conduction, together with a maximum dissipation postulate. In the absence of internal heat sources, the first law of thermodynamics is

$$\dot{T} = \frac{1}{\rho c_h}\Big(\text{div } (k\nabla T) + \mathcal{H} + \mathcal{D}_{mech}\Big), \tag{111}$$

where c_h is the specific heat at constant values of strain and internal variables, eq. (56), k the thermal conductivity, eq. (67), $\mathcal{D}_{mech}$ is the mechanical dissipation power,

$$\mathcal{D}_{mech} = \boldsymbol{\sigma} \cdot \dot{\boldsymbol{\epsilon}}_p + R(\widehat{\rho})^{\cdot} = \hat{\boldsymbol{\sigma}} \cdot \dot{\boldsymbol{\epsilon}}_p, \tag{112}$$

and $\mathcal{H}$ is the non-dissipative elastic-plastic heating

$$\mathcal{H} = T\left[\frac{\partial^2 \psi}{\partial T \partial \boldsymbol{\epsilon}_e} \cdot \dot{\boldsymbol{\epsilon}}_e + \frac{\partial^2 \psi}{\partial T \partial \widehat{\rho}}(\widehat{\rho})^{\cdot}\right]. \tag{113}$$

The first term inside the parenthesis describes the piezocaloric effect. The second part is a coupling term between the temperature and the internal variable (relative density). It is common for plasticity models [55] to replace the mechanical dissipation term with

$$\mathcal{D}_{mech} = \mathcal{X}\hat{\boldsymbol{\sigma}} \cdot \dot{\boldsymbol{\epsilon}}, \tag{114}$$

where $\mathcal{X}$ is sometimes called Quinney-Taylor coefficient and lies between 0.85 and 0.95. This factor was introduced as it was found

in experiments [58] that the heating associated with the plastic flow is roughly 0.9 times the rate of plastic working. If the plastic strain becomes very large, the Quinney-Taylor factor approaching unity, so that eq. (114) reduces to eq. (112). However, the mechanical dissipation plays only a negligible role in high temperature applications. In the case of ceramic sintering, a substantial amount of heat is transferred to the system from outside (for instance, the ceramics is left 30 min in the oven at about 1200° C), whereas the plastic deformation of the body occurs at a relatively slow pace. This heat transfer is far larger than the heating introduced by the piezocaloric effect or the plastic heating. It is therefore reasonable to neglect these terms (the mechanical dissipation and the non-dissipative elastoplastic heating) and assume $\mathcal{X} = 0$, which leads to a system where temperature evolution is uncoupled from plastic flow. Then, eq. (111) reduces to:

$$\dot{T} = \frac{1}{\rho c_h} \operatorname{div}\,(k \nabla T). \tag{115}$$

7.2 Temperature effect on the yield surface

At high temperature, a significant thermal softening effect occurs, which is modelled through a variation of the parameter p_c, which is assumed to follow the rule

$$p_c(\widehat{\rho}, \sigma_m, T) = f_T(T)\, p_c(\widehat{\rho}, \sigma_m), \tag{116}$$

with $f_T(T)$ being a function steadily decreasing with temperature, defined as equal to one at the reference temperature. For high temperatures, over about $800°C$ and slow deformation rates, the material exhibits creep as dominant deformation mechanism [3, 27], and its strength is assumed to be negligible at this temperature, so that

$$f_T(T) = \left\langle 1 - \frac{T}{T_{C1}} \right\rangle^{b_1} + C_T, \tag{117}$$

where the Macaulay bracket has been used and $T_{C1} = 800°C$ and $C_T = 0.0001$ and $b_1 = 0.9$.

7.3 Grain growth

The sintering process is usually accompanied by grain coarsening [51]. As grain coarsening has some effect on the process kinetics it should be considered. The grain growth occurring during sintering is assumed to follow an exponential law that models the evolution of the average grain size, as described in [59] and [30], namely

$$\dot{R} = \frac{\gamma_b M_{gc}}{4R}, \qquad M_{gc} = M_{gc0} \exp\left(\frac{-Q_{gc}}{R_g T}\right), \tag{118}$$

where the constant M_{gc0} is taken from [59] to be $2.25 m^2 s/kg$ and the activation energy for grain coarsening Q_{gc} is similar to the viscous activation energy. The value for the grain boundary energy γ_b is taken from the same source and is equal to $1.10 J/m^2$. The values of the activation energies, to be used for the model, can be obtained by fitting them to experimental results. The procedure is described in section 8.3.1.

7.4 Viscosity

The shrinkage of the ceramics under thermal load during sintering is essentially a time-dependent process, so that the previously developed time-independent model has to be enhanced to describe rate-dependent effects, thus introducing viscosity. There are several possibilities to introduce viscous behavior, for instance using the Coble [12] or the Nabarro-Herring [50] creep model. Olevsky [46] introduces a model based on a dissipation potential that can be derived from a strain energy function, the viscous models proposed by [8, 50] are found to yield a better fit to experiments

performed in [60, 61]. The viscosity η_v depends on the temperature, density and grain size and is assumed to be multiplicative as

$$\eta_v = \eta_{v1} \cdot \eta_{v2}(R) \cdot \eta_{v3}(T), \tag{119}$$

where η_{v1} is a constant and η_{v2} and η_{v3} are respectively functions of the radius R of the particles and of the temperature. In particular, introducing the initial radius R_0 of the particles, the function η_{v2} is assumed in the form

$$\eta_{v2}(R) = \left(\frac{R}{R_0}\right)^w, \tag{120}$$

where the exponent w is equal to 3 for an assumed mechanism of grain boundary diffusion, while it is equal to 2 for lattice diffusion [50]. Finally the temperature dependence in the law (119) follows an Arrhenius type law (compare with [60]):

$$\eta_{v3}(T) = e^{\frac{Q_E}{R_g T}}, \tag{121}$$

where Q_E is the activation energy for the viscosity and R_g the universal gas constant ($8.314\ J/(molK)$).

In conclusion, the complete function governing the viscosity is

$$\eta_v = \eta_{v1} \left(\frac{R}{R_0}\right)^w e^{\frac{Q_E}{R_g T}}. \tag{122}$$

The values of the constants were fitted against a sintering curve obtained from one dilatometric test, which is described in section 8.3.1.

8 Implementation and Validation

A model for the sintering process was developed within the scope of the previous chapter. It is the aim of this study to apply the model and implement it as a numerical simulation. This way it can be validated and subsequently used for the simulation and optimization of sintering processes.

8.1 List of equations

Over the course of the previous chapters, a variety of equations were used. An overview of the equations needed to implement the model as a numerical solution is shown here:

$$
\begin{aligned}
\boldsymbol{\epsilon} &= \boldsymbol{\epsilon}_e + \boldsymbol{\epsilon}_p \\
\dot{\boldsymbol{\epsilon}} &= \dot{\boldsymbol{\epsilon}}^{el} + \dot{\boldsymbol{\epsilon}}^{p} \\
\boldsymbol{\sigma} &= \mathbb{C} : \boldsymbol{\epsilon}^{el} - K_b \alpha_0 \left(T - T_0\right) \boldsymbol{I} \\
\sigma_s &= -3.224 \frac{\gamma_s}{L} \left(\frac{\widehat{\rho}}{1-\widehat{\rho}} \right)^{\frac{1}{3}} \\
\hat{\boldsymbol{\sigma}} &= \boldsymbol{\sigma} + \sigma_s \boldsymbol{I} \\
\dot{\boldsymbol{\epsilon}}^{vp} &= \frac{1}{\eta_v} \left\langle \mathcal{F}(\hat{\boldsymbol{\sigma}}, \widehat{\rho}) \right\rangle \frac{\frac{\partial \mathcal{F}(\hat{\boldsymbol{\sigma}}, \widehat{\rho})}{\partial \boldsymbol{\sigma}}}{\left\| \frac{\partial \mathcal{F}(\hat{\boldsymbol{\sigma}}, \widehat{\rho})}{\partial \boldsymbol{\sigma}} \right\|} \\
\eta_v &= \eta_{v1} (\frac{R}{R_0})^w \cdot e^{\frac{Q_E}{R_g T}} \\
\dot{R} &= \frac{\gamma_b M_{gc}}{4R}, \\
M_{gc} &= M_{gc0} \exp\left(\frac{-Q_{gc}}{R_g T} \right)
\end{aligned}
\tag{123}
$$

$$
\begin{aligned}
p_c(\widehat{\rho},\sigma_m) &= f_T(T)\,\sigma_m\,\frac{(-530+(619+25\pi-719\widehat{\rho})\sqrt{\frac{\widehat{\rho}-1}{\pi-4}}+530\widehat{\rho})}{210\sqrt{3}(\widehat{\rho}-1)}\\
M &= \frac{\sqrt{3}\sigma_m A_c}{2}\frac{1}{p_c\sqrt{[\frac{c}{p_c+c}-(\frac{c}{p_c+c})^m][2(1-\alpha_{bp})(\frac{c}{p_c+c})+\alpha_{bp}]}}\\
f_T(T) &= \begin{cases}\left(1-\frac{T}{T_{C1}}\right)^{b1} & \text{if} \quad T<T_{C1}\\ C_T & \text{if} \quad T>T_{C1},\end{cases}\\
\dot{T} &= \frac{1}{\rho c}\Big(\text{div }(\lambda_c \text{grad})T+\mathcal{H}-\mathcal{D}_{mech})\Big), \text{with}\\
\mathcal{F}(\boldsymbol{\sigma},M,p_c,c) &= F(p,M,p_c,c)+q\,g(\Theta_c,\gamma,\beta),\\
p &= -\frac{1}{3}\,\text{tr}\,\boldsymbol{\sigma}\\
q &= \sqrt{\frac{3}{2}\,\text{dev}(\boldsymbol{\sigma}):\text{dev}(\boldsymbol{\sigma})}\\
F(p,M,p_c,c) &= -Mp_c\sqrt{[\Phi_{bp}-(\Phi_{bp})^m][2(1-\alpha_{bp})\Phi_{bp}+\alpha_{bp}]},\\
\Phi_{bp} &= \frac{p+c}{p_c+c},\\
g(\Theta_c) &= \cos\left[\beta_{bp}\frac{\pi}{6}-\frac{1}{3}\cos^{-1}(\gamma_{bp}cos(3\Theta_c))\right].
\end{aligned}
\tag{124}
$$

8.2 Implementation of the numerical model

The material model developed in the previous Sections was implemented in Abaqus 6.13 (Dassault Systèmes SIMULIA Corp., Johnston (RI), USA) through a UMAT created with AceGen [36]. The main equation that is solved over the whole domain is eq. (59). The Finite Element is used to solve it (for more information see e.g. [5, 14, 32, 55]. For a finite element solution a weak form of this equation is solved numerically. An implicit scheme was used for the yield function, as explained in [57]. The viscoplastic deformation is evaluated using a return-mapping algorithm (as described in [14, 54, 55]), which was implemented taking advantage of the Automatic Differentiation technique [37, 57], to obtain the derivatives (first and second) needed in the algorithm. A consistent tangent matrix for the local Newton method for plasticity was obtained (as described in [14, 43]), without explicitly calculating cumbersome derivatives. The viscosity is implemented using a Perzyna [47] type approach, as described in Section 4. As the model uses logarithmic strains, and finite deformation, the 'Nlgeom' option of Abaqus was used, which provides logarithmic strains as the input for the user material routine and uses finite deformation kinematics. The calibration of the yield function, using nominal stress, is described in section 8.3. For the solution of the global scheme, a separated Newton algorithm was used, in which the coupling terms of the global jacobian matrix (the entries that are a result of differentiation with respect to both displacement and temperature) are set to zero (see e.g. [44, 55]). This can be justified because the problem is weakly coupled 7.1, and computational cost is strongly reduced. The Newton technique was modified using a line search method, to improve convergence. Note that the general accuracy of the solution is not changed by using the separated solution scheme, while only the rate of convergence is slightly affected.

For the thermal part of the situation (see Chapter 7.1) the

temperature evolution model that is implemented in Abaqus suffices, as it based on the equations. The mechanical model is not implemented in Abaqus and thus needs to be implemented as a UMAT. The following algorithm was implemented:

The experimental setup described in Section 8.5 was modelled in Abaqus, where the mold and the stamp are modelled as analytical rigid bodies and the displacement is imposed on the stamp. To model the furnace environment, the temperature curve is imposed on the boundaries of the green body, obtained in a first step through modelling of cold powder compaction.

1. given: logarithmic strains $\boldsymbol{\epsilon}^n$ and plastic strains from previous step $\boldsymbol{\epsilon}_p^n$ at time t_n:
   $\boldsymbol{\epsilon}_p^{n+1}$=$\boldsymbol{\epsilon}_p^n$

2. calculate elastic strain:

   $$\boldsymbol{\epsilon}_e^{n+1} = \boldsymbol{\epsilon}^{n+1} - \boldsymbol{\epsilon}_p^{n+1}$$

3. calculate stress-strain relationships:

   $$\boldsymbol{\sigma} = \rho \frac{\partial \psi(\boldsymbol{\epsilon}_e, T, \widehat{\rho})}{\partial \boldsymbol{\epsilon}_e}$$
   $$\hat{\boldsymbol{\sigma}} = \boldsymbol{\sigma} + \sigma_s \boldsymbol{I}$$

4. check if plastic step:
   IF: $\mathcal{F}(\hat{\boldsymbol{\sigma}}, M, p_c, c)$ <= 0:EXIT
   ELSE: calculate residual Vector $\boldsymbol{R}$:
   initialize: k=0;

   $$\boldsymbol{R}^{(k)} = \begin{Bmatrix} \boldsymbol{\epsilon}_p^{n+1(k)} - \boldsymbol{\epsilon}_p^n - \frac{\Delta t}{\eta_v} \langle \mathcal{F}(\hat{\boldsymbol{\sigma}}, \widehat{\rho}) \rangle \mathcal{P} \\ \widehat{\rho}^{n+1(k)} - \widehat{\rho}^n + \widehat{\rho}^n \frac{\Delta t}{\eta_v} \langle \mathcal{F}(\hat{\boldsymbol{\sigma}}, \widehat{\rho}) \rangle \mathcal{P} \end{Bmatrix}$$
   with $\mathcal{P} = \dfrac{\frac{\partial \mathcal{F}(\hat{\boldsymbol{\sigma}}, \widehat{\rho})}{\partial \boldsymbol{\sigma}}}{\left\| \frac{\partial \mathcal{F}(\hat{\boldsymbol{\sigma}}, \widehat{\rho})}{\partial \boldsymbol{\sigma}} \right\|}$

5. IF $|\boldsymbol{R}|$ <= 10^{-9}
   THEN: set $\boldsymbol{\epsilon}_p^{n+1} = \boldsymbol{\epsilon}_p^{n+1(k)}$; $\widehat{\rho}^{n+1} = \widehat{\rho}^{n+1(k)}$
   EXIT;
   ELSE: use Newton's method to find a solution

Box 1: Viscoplastic return mapping as implemented in Umat.

1. initialize: $i = 0$;
   initialize: Vector of unknowns $\boldsymbol{h}^{(0)} = \{\boldsymbol{\epsilon}_p^{n+1(0)}, \widehat{\rho}^{n+1(0)}\}$

2. Calculate the increment for the vector of unknowns

   $$\Delta \boldsymbol{h}^i = -\left(\frac{\partial \boldsymbol{R}}{\partial \boldsymbol{h}}\right) \boldsymbol{R}(\boldsymbol{h}^i)$$

3. Calculate the new vector of unknowns

   $$\boldsymbol{h}^{i+1} = \boldsymbol{h}^i + \Delta \boldsymbol{h}^i$$

4. Check for convergence
   IF: $|\Delta \boldsymbol{h}^i| \leq 10^{-9}$ Then: EXIT
   Else:
   Return to Step 2

Box 2: Algorithm for local Newton's method.

8.3 Calibration

Experiments have been performed to calibrate and subsequently validate the material model. In particular, the calibration of the viscosity parameters of the model has been conducted with a dilatometric test, while the yield function parameters have been evaluated on the basis of available experiments [9]. Finally, validation of the model performance is performed through a comparison between model predictions and the shrinking of a specially designed ceramic piece, measured during sintering.

8.3.1 Calibration of the viscosity parameters

The sintering curve can be obtained using a dilatometer, a standard equipment in laboratories dealing with ceramics. Using a special dilatometer, a method has been proposed for experimentally determining the viscosities and activation energies for pure alumina [60, 61], thouugh a long series of experiments. Instead of this complex procedure, the viscosity parameters of the proposed model have been estimated through a comparison between the results from dilatometer tests and numerical simulations in which only a single element has been used. The temperature was assigned as a constraint on all nodes, following the temperature curve of the dilatometer. This procedure can be justified because of the very small dimensions of the specimen, which does not possess a large thermal capacity. The values for the viscosity constant η_{v1} and for the activation energies Q_E and Q_{gc} were found by running simulations with different values and iterating towards an optimal fit. This simplified approach was chosen because experimental values for the activation energies of traditional ceramics are not available. It was assumed that the activation energies for grain coarsening and viscosity are equal, an assumption based on the fact that these values have been found very similar on ceramic materials (but different from that addressed in the present study [60]). Experimental data for mechanical

properties are rare, as their determination is not straightforward [23] and often not of interest for the involved industries. However, a yield strength ranging between 125 MPa and 250 MPa is provided in [19], so that $\sigma_m = 150$ MPa has been assumed. Aluminum silicate spray dried powder (Sacmi I20087) was used, with a theoretical density (when containing no pores) of about 2.375 g/cm^3. To obtain the sintering curve from the powder, a dilatometer (TAinstruments DIL-831) was used at a heating rate of 30°C per minute, equal to the heating rate employed in industrial furnaces. Data in Figure 22 have been plotted after the strain due to thermal expansion was subtracted, to yield a graph that is corrected for thermal expansion, which was measured in a previous trial, with a completely sintered piece. The best fit was found for the viscosity constant $\eta_{v1} = 1 \cdot 10^{-8}$ MPa $\cdot$ s and activation energies $Q_E = Q_{gc}$=340 kJ/mol.

8.3.2 Calibration of the yield function parameters

The Bigoni Piccolroaz yield function, eq. (76), requires the determination of seven parameters. Using the previously developed micromechanical model, the number of unknown material constants can be reduced to four. During powder compaction and sintering, in most of the cases the body is under a compressive load. Therefore, the lode angle-dependence is of a minor importance and is therefore neglected, so that parameters β_{bp} and γ_{bp} are set to zero. The parameters α_{bp} and M determine the shape in the p-q plane. The value for $m = 4.38$ has been deduced from [9], while α_{bp} is chosen to be equal to the unit, as in the simple case of the modified Cam-Clay model [7]. The size of the yield surface in the pq- plane is determined by p_c, c and M, which are functions of the relative density. The yield surface evolves as the density grows. The evolution is shown in Figure 23.

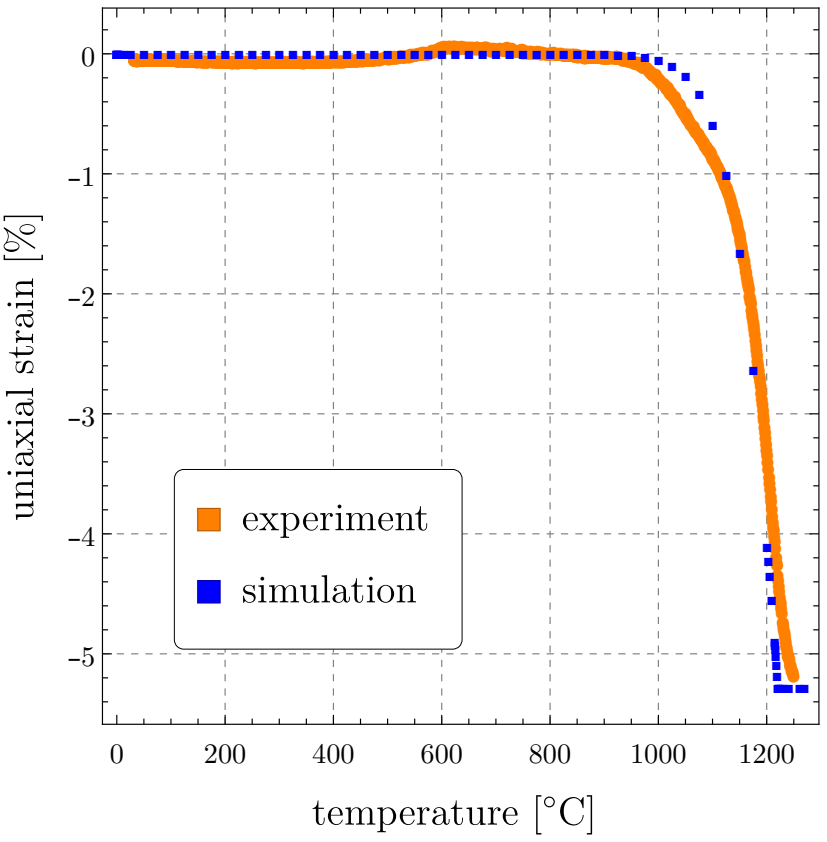

Figure 22: Activation energies and the viscosity constants have been determined with repeated numerical simulations of a dilatometer test, until a good fit has been found (illustrated in the figure) with experiments.

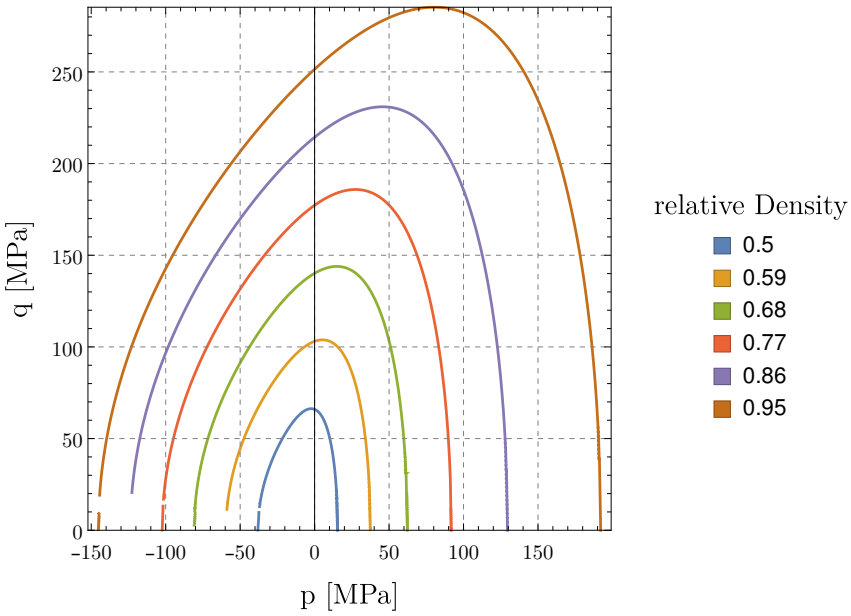

Figure 23: The BP yield surface evolution with respect to the relative density, for a porcellain stoneware ceramic (aluminum silicate spray dried powder). The parameters defining the yield surface are $\alpha_{bp} = 1$, $m = 4.38$,$\gamma_{bp} = 0$, $\beta_{bp} = 0$, σ_m =150MPa

8.4 Material parameters used for the examples

In summary, the values of the material parameters which were identified for the presented model are listed in Table 1.

Material Parameters	Values
R_0: Initial particle radius	11.24 10^{-6}m
γ_s: Surface energy	1.10 J/m^2
L: Constant for the porous addition to the free energy	$2\,R_0$
Q_E: Viscous activation energy	354 kJ/mol
M_{gc0}: Grain boundary mobility coefficient	2.25 m^{2}s/kg
Q_{gc}: Grain boundary mobility activation Energy	354 kJ/mol
E: Young's modulus	5000 MPa
$\mathcal{X}$: Taylor Quinney Coefficient	0.0
σ_m: Compressive strength of the fully dense material	150MPa
w: Material constant for the viscosity law	2 (lattice diffusion)
R_g: Gas constant	8.314 $J/(molK)$
T_{C1}: Temperature constant for thermal softening law	800°C
T_{C2}: Constant for thermal softening law	0.0001
b_1: Constant for thermal softening law	0.9
ρ_0: inital density	0.38
η_{v1}: viscosity constant	10^{-8} MPa ·s
m: BP Parameter	4.38
β: BP Parameter	0
γ: BP Parameter	0
α: BP Parameter	1
μ: Coulomb friction coefficient for die/stamp	0.4

Table 1: Material values used for the simulations

8.5 Experimental validation

Validation of the model has been obtained by referring to the sintering of a special green piece, namely, a profiled tile. It is possible to introduce some complexity to a floor tile by using a special tool with varying heights (as sketched in Figure 24), thus obtaining a green with zones of different height and therefore density. Before sintering, this profiled geometry has to be pressed from powder, using a tool that was manufactured for this specific purpose (Fig. 24). The dimension before pressing was 330mm $\times$ 125mm, with an initial uniform thickness of 22mm. The profiled tile was pressed with a symmetric tool, to avoid lateral loads during stamping, as sketched in Figure 24.

Twenty of the profiled tiles were formed and their density measured in the Laboratory of Sacmi international group for manufacturing machines and complete plants for the Ceramics, Packaging, Food industries and Automation (located at Imola, Italy). All the ceramic pieces were found to be so closely similar in the density distributions, that it was decided to fire only 6 greens. Three groups of two greens were fired respectively at temperatures of $1100°C$, $1150°C$ and $1200°C$, by adopting the heating cycle shown in Figure 25.

The density variation before and after sintering was measured using the purpose-made X-ray Line Scanner (of the Sacmi Continua+ line, manufactured by Microtec Srl, Bressanone, Italy) at the Sacmi laboratory. While the thickness changes abruptly, creating a tile with three rather distinct heights (about 9.8mm, 10.2mm and 10.7mm), the density varies less abruptly, as can be seen in Figure 28a. The density distribution measured on the pair of tiles subject to the same treatment was found so similar that the experimental data were almost superimposed and only one experiment for each pair is reported below.

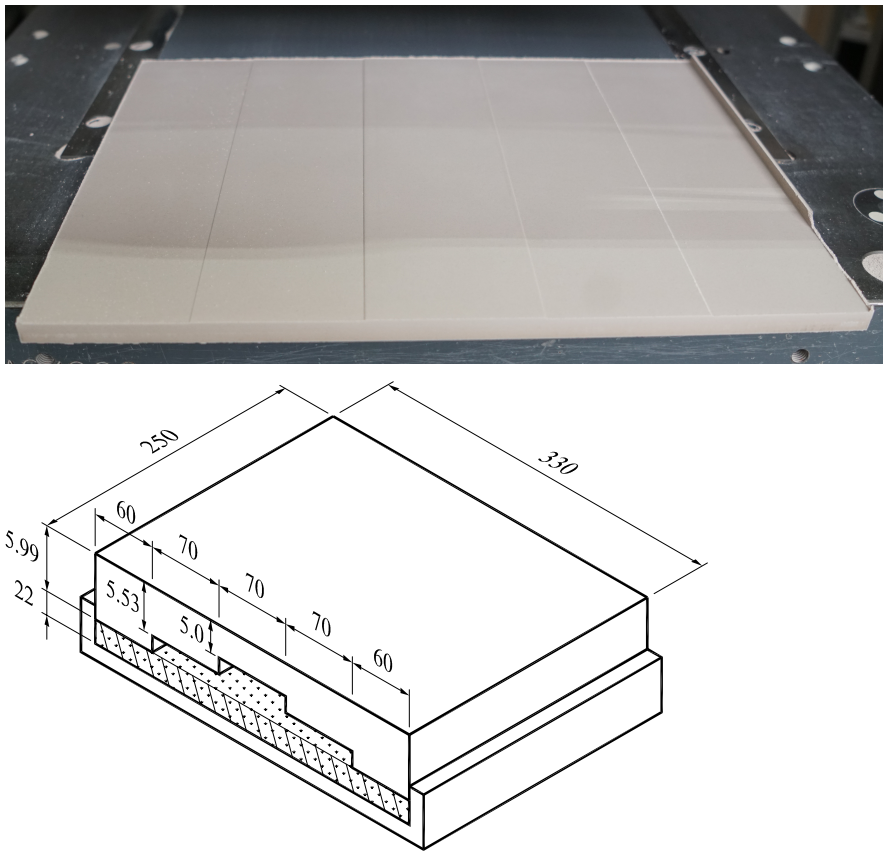

Figure 24: Upper part: The green body, with zones of different height and therefore density, used for sintering and density measurements. The green was formed with a tool, which was manufactured with three different heights. Lower part: sketch of the mold used to form the green body (not true to scale).

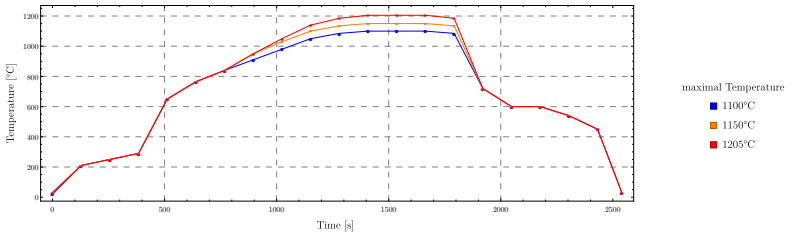

Figure 25: Sintering is obtained moving the green through a continuous oven (Sacmi Forni S.pA. EUP 130) across different temperature zones, so that the time-temperature curve shown above is applied.

Figure 26: For density measurements an X-Ray scanner from the Sacmi CONTINUA+ line was used, shown in the photo.

8.6 Simulation of the forming and sintering of the ceramic plate with different densities

The stamp and mold for powder forming were modelled as rigid bodies in contact with Coulomb friction (coefficient equal to 0.4). The powder was initally considered of uniform height (22mm) and homogeneous relative density (0.38), as in the experimental setup. The stamp is then displaced by $\Delta H = 12.6$ mm, pressing the body in the desired shape. Powder pressing is usually modelled as a rate-independent process [48], so that for the powder pressing part of the simulation, the viscosity was set to a constant and low value, to come close to the limit of rate-independent plasticity. For the sintering the viscosity description reported in section 7.4 was used and the temperature curve of the oven was prescribed on the boundaries of the ceramic body. The simulated geometry is shown in Figure 27, where the undeformed and deformed meshes are reported. The figure clearly shows the large

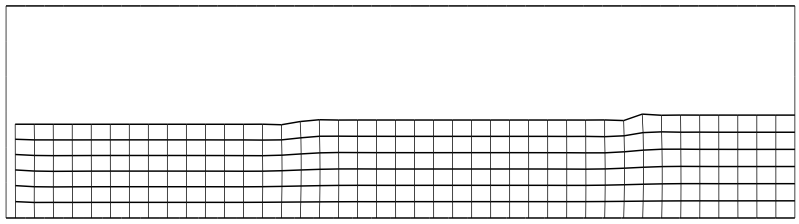

Figure 27: The mesh of the modelled powder in its inital state before (without mesh) and after pressing, after it is released from the mold the mold (with mesh). Just one half the piece was simulated, due to symmetry. The figure is scaled by 200% in height direction, to make the contour change more visible.

strain suffered by the powder during compaction and the presence of a modest spring back effect, which is limited because of the flat geometry of the sample. The springback works in such a way, that the tile increases in height, after release but decreases a little in width.

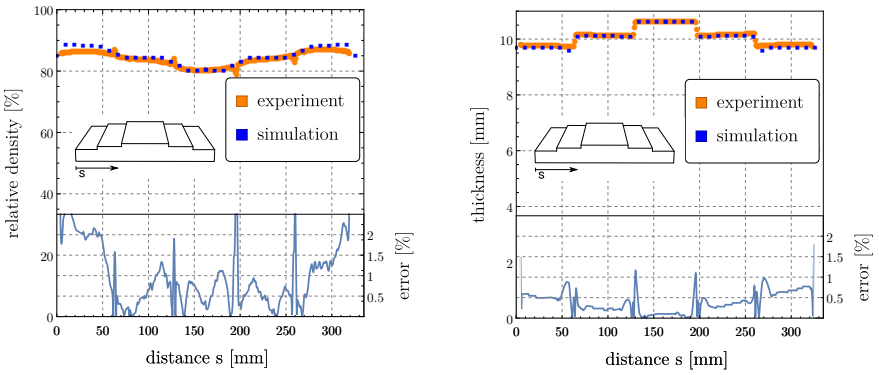

(a) Density variation (b) Thickness variation

Figure 28: Density and thickness variation of the green, measured by an X-ray scan, and compared to the model prediction through numerical simulation

Measurements of density and thickness are shown and compared to the simulation results in Figs. 28 and 31.

These figures prove the validity of the model, which is capable of reproducing the entire compaction and sintering process of a ceramic granulate with an excellent precision, so that the percent errors (reported in the lower parts of the graphs) are below 4% at maximum and for most of the part below 2% .

The distortion and the density distribution simulated in the ceramic piece after the entire process of compaction and sintering is shown in Figure 32, demonstrating the strong effect of sintering on the deformation of the tile. Finally, a photograph of the sintered tile is shown in Figure 33 with superimposed the deformed mesh obtained after the simulated compaction and sintering process. Both Figs. 32 and 33 again demonstrate the excellent predictive capabilities of the mechanical model.

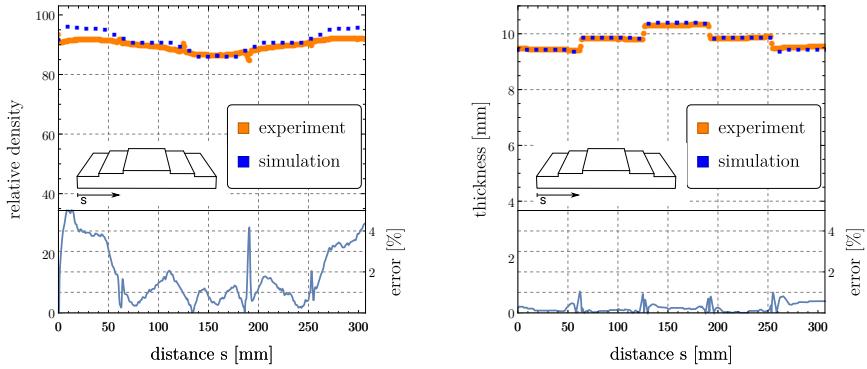

(a) Density variation (b) Thickness variation

Figure 29: Density and thickness variation of the ceramic piece after firing at 1100° measured by an X-ray scan, and compared to the model prediction through numerical simulation

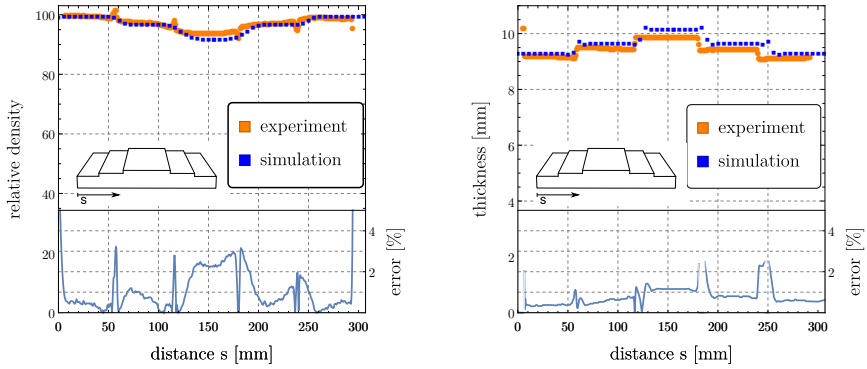

Figure 30: Density and thickness variation of the ceramic piece after firing at 1150° (bottom) measured by an X-ray scan, and compared to the model prediction through numerical simulation

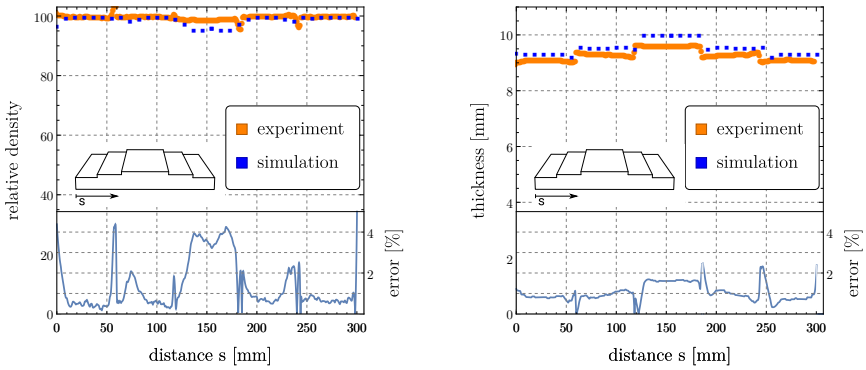

(a) Density variation

(b) Thickness variation

Figure 31: Density and thickness variation of the ceramic piece after firing at 1200° (bottom) measured by an X-ray scan, and compared to the model prediction through numerical simulation

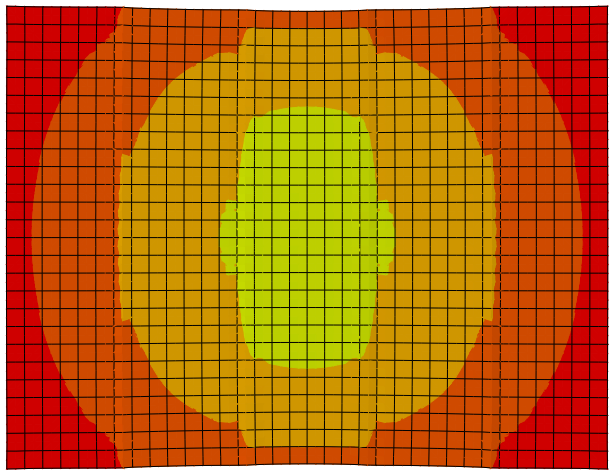

Figure 32: The geometry and the density distribution of the ceramic piece after a simulated process of compaction and firing at 1200 ° (only one fourth of the piece was simulated - the result was mirrored along the two symmetry axis).

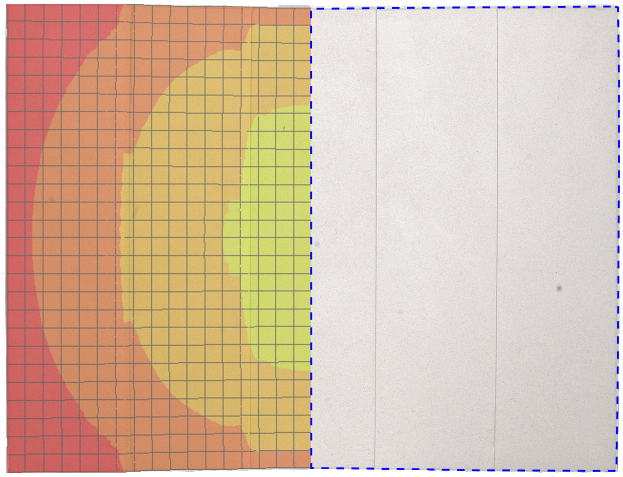

Figure 33: The simulation of the formed and fired ceramic piece (on the left) compared to a photo of the real ceramic piece, sintered at 1200°C (on the right, with the contour marked in blue). The qualitative trend of the distortion of the boundary is well reproduced by the simulation, which also correctly captures also the pronounced shrinkage at the middle of the ceramic piece.

8.7 Conclusion

It has been shown that a thermomechanical model can be formulated, implemented and calibrated to provide a computational tool for the simulation of the entire process of ceramic production, starting from the cold pressing of a granulate and ending with the subsequent non-isothermal firing and sintering.

Compared with the results of *ad hoc* performed experiments, the model predictions provide an accurate description of the density distribution and the shape distortion suffered by the piece during the production process.

Although the developed model is based on several simplificative assumptions and the lack of experimental data (inherent to the extreme conditions to which a ceramic piece is exposed) has precluded a fine calibration of model parameter, it is believed that the presented results show that mechanical modelling is a valuable alternative to the empirical processes still often in use in the ceramic industry.

References

[1] M. Abouaf, J.-L. Chenot, G. Raisson, P. Bauduin, A. M, C. J.L., R. G., and B. P. "Finite element simulation of hot isostatic pressing of metal powders". In: *International Journal for Numerical Methods in Engineering* 25.February 1987 (1988), pp. 191–212.

[2] L. P. Argani, D. Misseroni, A. Piccolroaz, D. Capuani, and D. Bigoni. "Plastically-driven variation of elastic stiffness in green bodies during powder compaction: Part II. Micromechanical modelling". In: *Journal of the European Ceramic Society* 36.9 (2016), pp. 2169–2174. DOI: 10.1016/j.jeurceramsoc.2016.02.012. arXiv: 1511.08914.

[3] M. F. Ashby and H. Frost. *Deformation-mechanism maps*. Cambridge University Engineering Dept., 1981.

[4] Y. BaÅ§ar and D. Weichert. *Nonlinear Continuum Mechanics of Solids*. Berlin, Heidelberg: Springer Berlin Heidelberg, 2000. DOI: 10.1007/978-3-662-04299-1.

[5] T. Belytschko, W. K. Liu, B. Moran, and K. Elkhodary. *Nonlinear Finite Elements for Continua and Structures*. 2nd editio. West Sussex: John Wiley & Sons, Ltd, 2014, p. 804.

[6] D. Bigoni. *Nonlinear Solid Mechanics*. Cambridge: Cambridge University Press, 2012. DOI: 10.1017/CBO9781139178938.

[7] D. Bigoni and A. Piccolroaz. "Yield criteria for quasibrittle and frictional materials". In: *International Journal of Solids and Structures* 41.11-12 (2004), pp. 2855–2878. DOI: 10.1016/j.ijsolstr.2003.12.024. arXiv: 1010.1823.

[8] R. K. Bordia and G. W. Scherer. "On constrained sintering-I. Constitutive model for a sintering body". In: *Acta Metallurgica* 36.9 (1988), pp. 2393–2397. DOI: 10.1016/0001-6160(88)90189-7.

[9] F. Bosi, A. Piccolroaz, M. Gei, F. D. Corso, A. Cocquio, and D. Bigoni. "Experimental investigation of the elastoplastic response of aluminum silicate spray dried powder during cold compaction". In: *Journal of the European Ceramic Society* 34.11 (2014), pp. 2633–2642. DOI: 10.1016/j.jeurceramsoc.2013.11.037. arXiv: arXiv:1405.0932v1.

[10] A. F. Bower. *Applied mechanics of solids*. Boca Raton, FL, USA: CRC Press, 2009.

[11] W. F. Chen. *Limit analysis and soil plasticity*. Ross, 2008.

[12] R. L. Coble. "A Model for Boundary Diffusion Controlled Creep in Polycrystalline Materials". In: *Journal of Applied Physics* 34.6 (1963), pp. 1679–1682. DOI: 10.1063/1.1702656. arXiv: arXiv:1011.1669v3.

[13] A. C. Cocks and I. C. Sinka. "Constitutive modelling of powder compaction - I. Theoretical concepts". In: *Mechanics of Materials* 39.4 (2007), pp. 392–403. DOI: 10.1016/j.mechmat.2006.09.003.

[14] E. A. de Souza Neto, D Perić, and D. R. J. Owen. *Computational Methods For Plasticity*. West Sussex: John Wiley & Sons, Ltd, 2008.

[15] I. Doghri. *Mechanics of Deformable Solids: Linear, Nonlinear, Analytical, and Computational Aspects*. Berlin: Springer, 2000.

[16] J. Duva and P. Crow. "The densification of powders by power-law creep during hot isostatic pressing". In: *Acta Metallurgica et Materialia* 40.1 (1992), pp. 31–35. DOI: 10.1016/0956-7151(92)90196-L.

[17] N. A. Fleck. "On the cold compaction of powders". In: *Journal of the Mechanics and Physics of Solids* 43.9 (1995), pp. 1409–1431. DOI: 10.1016/0022-5096(95)00039-L.

[18] N. A. Fleck, L. T. Kuhn, and R. T. McMeeking. "Yielding of metal powder by bonded contacts". In: *Journal of Me* 40.5 (1992).

[19] C. Fragassa, A. Pavlovic, and F. Ubertini. "Experimental Evaluation of Pyroclastic Deformation on Mechanical Properties of Grès Porcelain Stoneware". In: 20 (2014).

[20] J. Frischkorn and S. Reese. "Simulation of powder metallurgical coating by radial axial ring rolling". In: *Pamm* 8.1 (2008), pp. 10525–10526. DOI: 10.1002/pamm.200810525.

[21] A. Gajo and D. Bigoni. "Elastoplastic coupling for thermo-elasto-plasticity at high temperature". In: *Geomechanics for Energy and the Environment* 4 (2015), pp. 29–38. DOI: 10.1016/j.gete.2015.09.001.

[22] L. Galuppi and L. Deseri. "Combined effects of interstitial and Laplace pressure in hot isostatic pressing of cylindrical specimens". In: *Journal of Mechanics of Materials and Structures* 9.1 (2014), pp. 51–86. DOI: 10.2140/jomms.2014.9.51.

[23] M. Gei, D. Bigoni, and S. Guicciardi. "Failure of silicon nitride under uniaxial compression at high temperature". In: *Mechanics of Materials* 36.4 (2004), pp. 335–345. DOI: 10.1016/S0167-6636(03)00063-2.

[24] R. M. German. *Sintering: from Empirical Observations to Scientific Principles*. Elsevier, 2014. DOI: 10.1016/C2012-0-00717-X.

[25] O. Guillon, J. Rödel, and R. K. Bordia. "Effect of green-state processing on the sintering stress and viscosity of alumina compacts". In: *Journal of the American Ceramic Society* 90.5 (2007), pp. 1637–1640. DOI: 10.1111/j.1551-2916.2007.01572.x.

[26] A. L. Gurson. “Continuum theory of ductile rupture by void nucleation and growth”. In: *Journal of Engineering Materials and Technology* 99.76 (1977), pp. 2–15.

[27] V. H. Hammond and D. M. Elzey. “Elevated temperature mechanical properties of partially sintered alumina”. In: *Composites Science and Technology* 64.10-11 (2004), pp. 1551–1563. DOI: 10.1016/j.compscitech.2003.11.013.

[28] A. S. Helle, K. E. Easterling, and M. F. Ashby. “Hot-isostatic pressing diagrams: New developments”. In: *Acta Metallurgica* 33.12 (1985), pp. 2163–2174. DOI: 10.1016/0001-6160(85)90177-4.

[29] R. Hill. “On constitutive inequalities for simple materialsâĂŤI”. In: *Journal of the Mechanics and Physics of Solids* 16.4 (1968), pp. 229–242. DOI: 10.1016/0022-5096(68)90031-8.

[30] M Hillert. “On the theory of normal and abnormal grain growth”. In: *Acta Metallurgica* 13.3 (1965). Ed. by Intergovernmental Panel on Climate Change, pp. 227–238. DOI: 10.1016/0001-6160(65)90200-2. arXiv: arXiv:1011.1669v3.

[31] C. H. Hsueh, A. G. Evans, R. M. Cannon, and R. J. Brook. “Viscoelastic stresses and sintering damage in heterogeneous powder compacts”. In: *Acta Metallurgica* 34.5 (1986), pp. 927–936. DOI: 10.1016/0001-6160(86)90066-0.

[32] T. J. R. Hughes. *The finite element method : linear static and dynamic finite element analysis*. Englewood Cliffs, NJ: Prentice-Hall, 1987.

[33] M. Itskov. *Tensor Algebra and Tensor Analysis for Engineers*. Mathematical Engineering. Berlin, Heidelberg: Springer Berlin Heidelberg, 2013. DOI: 10.1007/978-3-642-30879-6.

[34] P. A. Kelly. *Mechanics Lecture Notes: An introduction to Solid Mechanics*.

[35] W. D. Kingery. "Sintering from Prehistoric Times to the Present". In: *Solid State Phenomena* 25-26 (1992), pp. 1–10. DOI: doi.org/10.4028/www.scientific.net/SSP.25-26.1.

[36] J. Korelc. "Automation of primal and sensitivity analysis of transient coupled problems". In: *Computational Mechanics* 44.5 (2009), pp. 631–649. DOI: 10.1007/s00466-009-0395-2.

[37] J. Korelc and P. Wriggers. *Automation of Finite Element Methods*. Cham: Springer International Publishing, 2016. DOI: 10.1007/978-3-319-39005-5.

[38] T. Kraft and H. Riedel. "Numerical simulation of solid state sintering; model and application". In: *Journal of the European Ceramic Society* 24.2 (2004), pp. 345–361. DOI: 10.1016/S0955-2219(03)00222-X.

[39] R. W. Lewis, D. T. Gethin, X. S. Yang, and R. C. Rowe. "A combined finite-discrete element method for simulating pharmaceutical powder tableting". In: *International Journal for Numerical Methods in Engineering* 62.7 (2005), pp. 853–869. DOI: 10.1002/nme.1287.

[40] J. Lubliner. *PLASTICITY THEORY Revised Edition*. 2005, p. 528.

[41] L. Mähler and K. Runesson. "Constitutive Modeling of Cold Compaction and Sintering of Hardmetal". In: *Journal of Engineering Materials and Technology* 125.2 (2003), p. 191. DOI: 10.1115/1.1491576.

[42] G. A. Maugin. *The thermomechanics of plasticity and fracture*. Cambridge: Cambridge University Press, 1992.

[43] C. Miehe, N. Apel, and M. Lambrecht. "Anisotropic additive plasticity in the logarithmic strain space: Modular kinematic formulation and implementation based on incremental minimization principles for standard materials". In: *Computer Methods in Applied Mechanics and Engineering* 191.47-48 (2002), pp. 5383–5425. DOI: 10.1016/S0045-7825(02)00438-3.

[44] C. Miehe. "Zur numerischen Behandlung thermomechanischer Prozesse". PhD thesis. University of Hannover, 1988, p. 195.

[45] R. Ogden. *Non-linear elastic deformations*. 1997, p. 532. DOI: 10.1016/0955-7997(84)90049-3.

[46] E. A. Olevsky. "Theory of sintering: from discrete to continuum". In: *Materials Science and Engineering: R: Reports* 23.2 (1998), pp. 41–100. DOI: 10.1016/S0927-796X(98)00009-6.

[47] P. Perzyna. "The constitutive equations for rate sensitive plastic materials". In: *Quarterly of Applied Mathematics* XX.4 (1963), pp. 321–332.

[48] A. Piccolroaz, D. Bigoni, and A. Gajo. "An elastoplastic framework for granular materials becoming cohesive through mechanical densification. Part I – small strain formulation". In: *European Journal of Mechanics - A/Solids* 25.2 (2006), pp. 334–357. DOI: 10.1016/j.euromechsol.2005.10.001.

[49] A. T. Procopio and A. Zavaliangos. "Simulation of multiaxial compaction of granular media from loose to high relative densities". In: *Journal of the Mechanics and Physics of Solids* 53.7 (2005), pp. 1523–1551. DOI: 10.1016/j.jmps.2005.02.007.

[50] M. Rahaman, L. Jonghe, and R. Brook. “Effect of Shear Stress on Sintering”. In: *Journal of the American Ceramic Society* 69.1 (1986), pp. 53–58. DOI: 10.1111/j.1151-2916.1986.tb04693.x.

[51] M. N. Rahaman. *Sintering of ceramics*. CRC Press, 2007.

[52] P. Redanz and N. A. Fleck. “The compaction of a random distribution of metal cylinders by the discrete element method”. In: *Acta Materialia* 49.20 (2001), pp. 4325–4335. DOI: 10.1016/S1359-6454(01)00298-1.

[53] C. Sansour and W. Wagner. “Viscoplasticity based on additive decomposition of logarithmic strain and unified constitutive equations - Theoretical and computational considerations with reference to shell applications”. In: *Computers and Structures* 81.15 (2003), pp. 1583–1594. DOI: 10.1016/S0045-7949(03)00149-4.

[54] J. C. Simo and T. J. R. Hughes. *Computational Inelasticity*. New York: Springer, 1998.

[55] J. C. Simo and C Miehe. “Associative coupled thermoplasticity at finite strains: Formulation, numerical analysis and implementation”. In: *Computer Methods in Applied Mechanics and Engineering* 98.1 (1992), pp. 41–104. DOI: 10.1016/0045-7825(92)90170-O.

[56] S. Stupkiewicz, A. Piccolroaz, and D. Bigoni. “Finite-strain formulation and FE implementation of a constitutive model for powder compaction”. In: *Computer Methods in Applied Mechanics and Engineering* 283 (2015), pp. 856–880. DOI: 10.1016/j.cma.2014.09.027.

[57] S. Stupkiewicz, R. Denzer, A. Piccolroaz, and D. Bigoni. “Implicit yield function formulation for granular andÂărock-like materials”. In: *Computational Mechanics* 54.5 (2014), pp. 1163–1173. DOI: 10.1007/s00466-014-1047-8.

[58] G. I. Taylor and H. Quinney. "The Latent Energy Remaining in a Metal after Cold Working". In: *Proceedings of the Royal Society A: Mathematical, Physical and Engineering Sciences* 143.849 (1934), pp. 307–326. DOI: 10.1098/rspa.1934.0004. arXiv: 0511310 [arXiv:cond-mat].

[59] A. Wonisch, T. Kraft, M. Moseler, and H. Riedel. "Effect of different particle size distributions on solid-state sintering: A microscopic simulation approach". In: *Journal of the American Ceramic Society* 92.7 (2009), pp. 1428–1434. DOI: 10.1111/j.1551-2916.2009.03012.x.

[60] R. Zuo and J. Rödel. "Temperature dependence of constitutive behaviour for solid-state sintering of alumina". In: *Acta Materialia* 52.10 (2004), pp. 3059–3067. DOI: 10.1016/j.actamat.2004.03.008.

[61] R. Zuo, E. Aulbach, and J. Rödel. "Experimental determination of sintering stresses and sintering viscosities". In: *Acta Materialia* 51.15 (2003), pp. 4563–4574. DOI: 10.1016/S1359-6454(03)00293-3.

An elastic-visco-plastic thermomechanical model for cold forming of ceramic powders and subsequent sintering is introduced and based on micromechanical modelling of the compaction process of granulates. Micromechanics is shown to yield an upper-bound estimate to the compaction curve of a granular material, which compares well with other models and finite element simulations. The parameters of the thermomechanical model are determined on the basis of available data and dilatometer experiments. Finally, after computer implementation, validation of the model is performed with a specially designed ceramic piece showing zones of different density. The mechanical model is found to accurately describe forming and sintering of stoneware ceramics and can therefore be used to analyze and optimize.

Daniel Kempen was born in Aachen, Germany on December 12th 1987. He studied Mechanical engineering in Aachen and graduated with a Master's degree focussing on numerical methods and simulation. He started this PhD degree at the University of Trento in 2015 with the financial support of a Marie Curie ITN grant. The main topic of the research is thermomechanical material models for production processes of ceramics.